

1      **High-level cognition during story listening is reflected in  
2      high-order dynamic correlations in neural activity patterns**

3      Lucy L. W. Owen<sup>1</sup>, Thomas H. Chang<sup>1,2</sup>, and Jeremy R. Manning<sup>1,†</sup>

<sup>1</sup>Department of Psychological and Brain Sciences,  
Dartmouth College, Hanover, NH

<sup>2</sup>Amazon.com, Seattle, WA

†Address correspondence to jeremy.r.manning@dartmouth.edu

4      June 9, 2021

5      **Abstract**

6      Our thoughts arise from coordinated patterns of interactions between brain structures that change  
7      with our ongoing experiences. High-order dynamic correlations in neural activity patterns reflect different  
8      subgraphs of the brain's functional connectome that display homologous lower-level dynamic correlations.  
9      We tested the hypothesis that high-level cognition is reflected in high-order dynamic correlations in brain  
10     activity patterns. We developed an approach to estimating high-order dynamic correlations in timeseries  
11     data, and we applied the approach to neuroimaging data collected as human participants either listened to  
12     a ten-minute story or listened to a temporally scrambled version of the story. We trained across-participant  
13     pattern classifiers to decode (in held-out data) when in the session each neural activity snapshot was  
14     collected. We found that classifiers trained to decode from high-order dynamic correlations yielded the best  
15     performance on data collected as participants listened to the (unscrambled) story. By contrast, classifiers  
16     trained to decode data from scrambled versions of the story yielded the best performance when they  
17     were trained using first-order dynamic correlations or non-correlational activity patterns. We suggest that  
18     as our thoughts become more complex, they are reflected in higher-order patterns of dynamic network  
19     interactions throughout the brain.

20     **Introduction**

21     A central goal in cognitive neuroscience is to elucidate the *neural code*: the mapping between (a) mental  
22     states or cognitive representations and (b) neural activity patterns. One means of testing models of the  
23     neural code is to ask how accurately that model is able to "translate" neural activity patterns into known  
24     (or hypothesized) mental states or cognitive representations (e.g., Haxby et al., 2001; Huth et al., 2016, 2012;  
25     Kamitani & Tong, 2005; Mitchell et al., 2008; Nishimoto et al., 2011; Norman et al., 2006; Pereira et al., 2018;  
26     Tong & Pratte, 2012). Training decoding models on different types of neural features (Fig. 1a) can also help to  
27     elucidate which specific aspects of neural activity patterns are informative about cognition and, by extension,  
28     which types of neural activity patterns might compose the neural code. For example, prior work has used  
29     region of interest analyses to estimate the anatomical locations of specific neural representations (e.g., Etzel  
30     et al., 2009), or to compare the relative contributions to the neural code of multivariate activity patterns

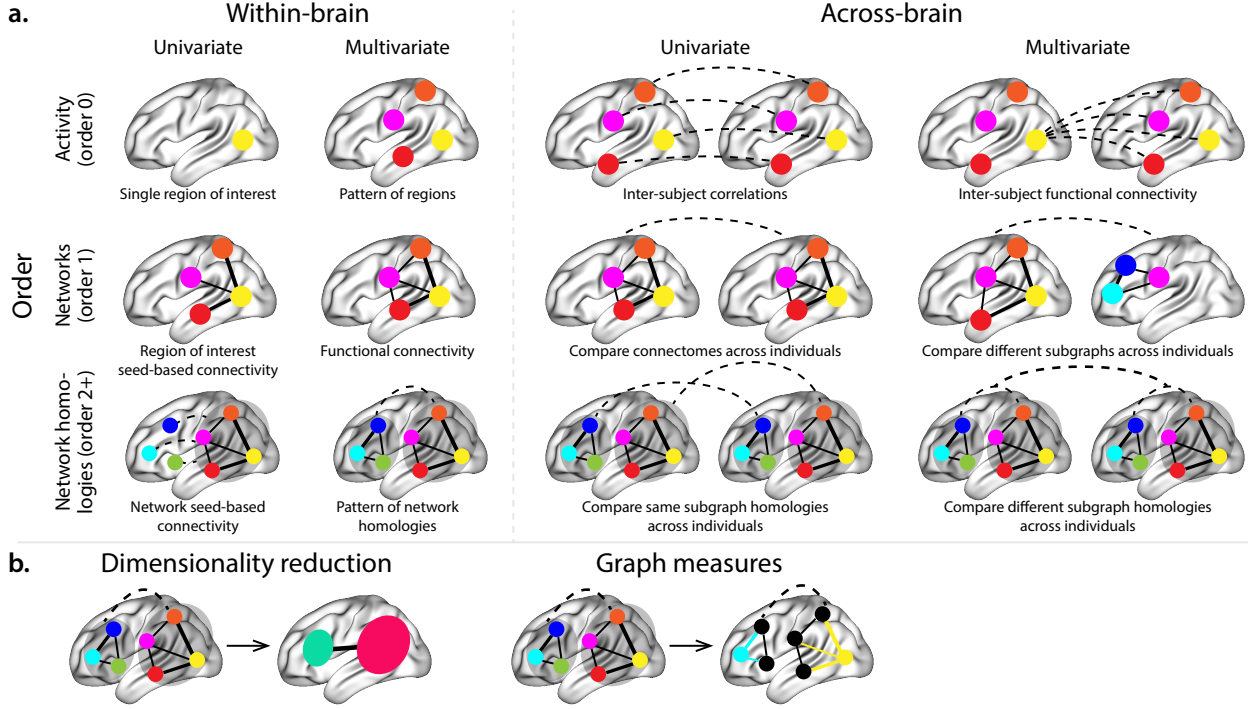


**Figure 1: Neural patterns. a. A space of neural features.** Within-brain analyses are carried out within a single brain, whereas across-brain analyses compare neural patterns across two or more individuals' brains. Univariate analyses characterize the activities of individual units (e.g., nodes, small networks, hierarchies of networks, etc.), whereas multivariate analyses characterize the patterns of activity across units. Order 0 patterns involve individual nodes; order 1 patterns involve node-node interactions; order 2 (and higher) patterns relate to interactions between homologous networks. Each of these patterns may be static (e.g., averaging over time) or dynamic. **b. Summarizing neural patterns.** To efficiently compute with complex neural patterns, it can be useful to characterize the patterns using summary measures. Dimensionality reduction algorithms project the patterns onto lower-dimensional spaces whose dimensions reflect weighted combinations or non-linear transformations of the dimensions in the original space. Graph measures characterize each unit's participation in its associated network.

31 versus dynamic correlations between neural activity patterns (e.g., Fong et al., 2019; Manning et al., 2018).

32 An emerging theme in this literature is that cognition is mediated by dynamic interactions between brain

33 structures (Bassett et al., 2006; Bressler & Kelso, 2001; Demertzi et al., 2019; Friston, 2000; Grossberg, 1988;

34 Lurie et al., 2018; Mack et al., 2017; McIntosh, 2000; Preti et al., 2017; Solomon et al., 2019; Sporns & Honey,

35 2006; Turk-Browne, 2013; Zou et al., 2019).

36 Studies of the neural code to date have primarily focused on univariate or multivariate neural pat-  
 37 terns (for review see Norman et al., 2006), or (more recently) on patterns of dynamic first-order corre-  
 38 lations (i.e., interactions between pairs of brain structures; Demertzi et al., 2019; Fong et al., 2019; Lurie et al.,  
 39 2018; Manning et al., 2018; Preti et al., 2017; Zou et al., 2019). What might the future of this line of work  
 40 hold? For example, is the neural code implemented through higher-order interactions between brain struc-

41 tures (e.g., see Reimann et al., 2017)? Second-order correlations reflect *homologous* patterns of correlation.  
42 In other words, if the dynamic patterns of correlations between two regions, *A* and *B*, are similar to those  
43 between two other regions, *C* and *D*, this would be reflected in the second-order correlations between (*A*–*B*)  
44 and (*C*–*D*). In this way, second-order correlations identify similarities and differences between subgraphs  
45 of the brain’s connectome. Analogously, third-order correlations reflect homologies between second-order  
46 correlations—i.e., homologous patterns of homologous interactions between brain regions. More generally,  
47 higher-order correlations reflect homologies between patterns of lower-order correlations. We can then ask:  
48 which “orders” of interaction are most reflective of high-level cognitive processes?

49 One reason one might expect to see homologous networks in a dataset is related to the notion that  
50 network dynamics reflect ongoing neural computations or cognitive processing (e.g., Beaty et al., 2016). If  
51 the nodes in two brain networks are interacting (within each network) in similar ways then, according to  
52 our characterization of network dynamics, we refer to the similarities between those patterns of interaction  
53 as higher-order correlations. When higher-order correlations are themselves changing over time, we can  
54 also attempt to capture and characterize those high-order dynamics.

55 Another central question pertains to the extent to which the neural code is carried by activity patterns  
56 that directly reflect ongoing cognition (e.g., following Haxby et al., 2001; Norman et al., 2006), versus the  
57 dynamic properties of the network structure itself, independent of specific activity patterns in any given  
58 set of regions (e.g., following Bassett et al., 2006). For example, graph measures such as centrality and  
59 degree (Bullmore & Sporns, 2009) may be used to estimate how a given brain structure is “communicating”  
60 with other structures, independently of the specific neural representations carried by those structures.  
61 If one considers a brain region’s position in the network (e.g., its eigenvector centrality) as a dynamic  
62 property, one can compare how the positions of different regions are correlated, and/or how those patterns  
63 of correlations change over time. We can also compute higher-order patterns in these correlations to  
64 characterize homologous subgraphs in the connectome that display similar changes in their constituent  
65 brain structures’ interactions with the rest of the brain.

66 To gain insights into the above aspects of the neural code, we developed a computational framework  
67 for estimating dynamic high-order correlations in timeseries data. This framework provides an important  
68 advance, in that it enables us to examine patterns of higher-order correlations that are computationally  
69 intractable to estimate via conventional methods. Given a multivariate timeseries, our framework pro-  
70 vides timepoint-by-timepoint estimates of the first-order correlations, second-order correlations, and so  
71 on. Our approach combines a kernel-based method for computing dynamic correlations in timeseries  
72 data with a dimensionality reduction step (Fig. 1b) that projects the resulting dynamic correlations into  
73 a low-dimensional space. We explored two dimensionality reduction approaches: principle components

74 analysis (PCA; Pearson, 1901), which preserves an approximately invertible transformation back to the  
75 original data (e.g., this follows related approaches taken by Gonzalez-Castillo et al., 2019; McIntosh & Jirsa,  
76 2019; Toker & Sommer, 2019); and a second non-invertible algorithm for computing dynamic patterns in  
77 eigenvector centrality (Landau, 1895). This latter approach characterizes correlations between each feature  
78 dimension's relative *position* in the network (at each moment in time) in favor of the specific activity histories  
79 of different features (also see Betzel et al., 2019; Reimann et al., 2017; Sizemore et al., 2018).

80 We validated our approach using synthetic data where the underlying correlations were known. We  
81 then applied our framework to a neuroimaging dataset collected as participants listened to either an audio  
82 recording of a ten-minute story, listened to a temporally scrambled version of the story, or underwent a  
83 resting state scan (Simony et al., 2016). Temporal scrambling has been used in a growing number of studies,  
84 largely by Uri Hasson's group, to identify brain regions that are sensitive to higher-order and longer-  
85 timescale information (e.g., cross-sensory integration, rich narrative meaning, complex situations, etc.)  
86 versus regions that are primarily sensitive to low-order (e.g., sensory) information. For example, Hasson et  
87 al. (2008) argues that when brain areas are sensitive to fine versus coarse temporal scrambling, this indicates  
88 that they are "higher order" in the sense that they process contextual information pertaining to further-  
89 away timepoints. By contrast, low-level regions, such as primary sensory cortices, do not meaningfully  
90 change their responses (after correcting for presentation order) even when the stimulus is scrambled at fine  
91 timescales.

92 We used a subset of the story listening and rest data to train across-participant classifiers to decode  
93 listening times (of groups of participants) using a blend of neural features (comprising neural activity  
94 patterns, as well as different orders of dynamic correlations between those patterns that were inferred  
95 using our computational framework). We found that both the PCA-based and eigenvector centrality-based  
96 approaches yielded neural patterns that could be used to decode accurately (i.e., well above chance). Both  
97 approaches also yielded the best decoding accuracy for data collected during (intact) story listening when  
98 high-order (PCA: second-order; eigenvector centrality: fourth-order) dynamic correlation patterns were  
99 included as features. When we trained classifiers on the scrambled stories or resting state data, only  
100 (relatively) lower-order dynamic patterns were informative to the decoders. Taken together, our results  
101 indicate that high-level cognition is supported by high-order dynamic patterns of communication between  
102 brain structures.

103 **Results**

104 We sought to understand whether high-level cognition is reflected in dynamic patterns of high-order  
105 correlations. To that end, we developed a computational framework for estimating the dynamics of stimulus-  
106 driven high-order correlations in multivariate timeseries data (see *Dynamic inter-subject functional connectivity*  
107 (*DISFC*) and *Dynamic higher-order correlations*). We evaluated the efficacy of this framework at recovering  
108 known patterns in several synthetic datasets (see *Synthetic data: simulating dynamic first-order correlations* and  
109 *Synthetic data: simulating dynamic higher-order correlations*). We then applied the framework to a public fMRI  
110 dataset collected as participants listened to an auditorily presented story, listened to a temporally scrambled  
111 version of the story, or underwent a resting state scan (see *Functional neuroimaging data collected during story*  
112 *listening*). We used the relative decoding accuracies of classifiers trained on different sets of neural features  
113 to estimate which types of features reflected ongoing cognitive processing.

114 **Recovering known dynamic correlations from synthetic data**

115 **Recovering dynamic first-order correlations**

116 We generated synthetic datasets that differed in how the underlying first-order correlations changed over  
117 time. For each dataset, we applied Equation 4 with a variety of kernel shapes and widths. We assessed how  
118 well the true underlying correlations at each timepoint matched the recovered correlations (Fig. 2). For every  
119 kernel and dataset we tested, our approach recovered the correlation dynamics we embedded into the data.  
120 However, the quality of these recoveries varied across different synthetic datasets in a kernel-dependent  
121 way.

122 In general, wide monotonic kernel shapes (Laplace, Gaussian), and wider kernels (within a shape),  
123 performed best when the correlations varied gradually from moment-to-moment (Figs. 2a, c, and d). In the  
124 extreme, as the rate of change in correlations approaches 0 (Fig. 2a), an infinitely wide kernel would exactly  
125 recover the Pearson's correlation (e.g., compare Eqns. 1 and 4).

126 When the correlation dynamics were unstructured in time (Fig. 2b), a Dirac  $\delta$  kernel (infinitely narrow)  
127 performed best. This is because, when every timepoint's correlations are independent of the correlations at  
128 every other timepoint, averaging data over time dilutes the available signal. Following a similar pattern,  
129 holding kernel shape fixed, narrower kernel parameters better recovered randomly varying correlations.

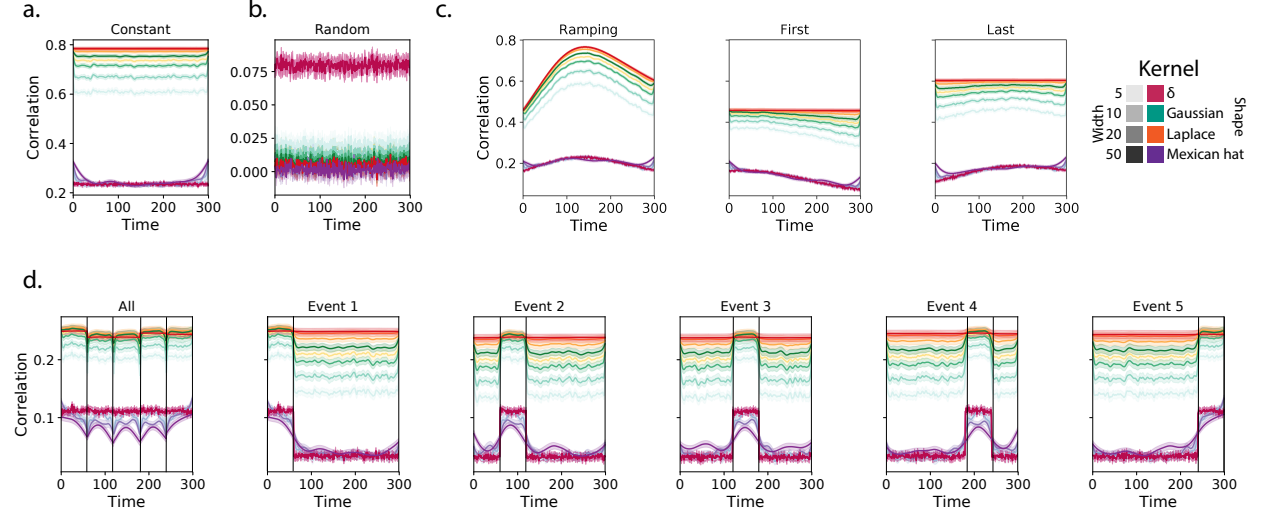


**Figure 2: Recovering known dynamic first-order correlations from synthetic data.** Each panel displays the average correlations between the vectorized upper triangles of the recovered correlation matrix at each timepoint and either the true underlying correlation at each timepoint or a reference correlation matrix. (The averages are taken across 10–100 different randomly generated synthetic datasets of [the each](#) given category, [each with  \$K = 50\$  features and  \$T = 300\$  timepoints](#).) Error ribbons denote 95% confidence intervals (taken across datasets). Different colors denote different kernel shapes, and the shading within each color family denotes the kernel width parameter. For a complete description of each synthetic dataset, see *Synthetic data: simulating dynamic first-order correlations*. **a. Constant correlations.** These datasets have a stable (unchanging) underlying correlation matrix. **b. Random correlations.** These datasets are generated using a new independently drawn correlation matrix at each new timepoint. **c. Ramping correlations.** These datasets are generated by smoothly varying the underlying correlations between the randomly drawn correlation matrices at the first and last timepoints. The left panel displays the correlations between the recovered dynamic correlations and the underlying ground truth correlations. The middle panel compares the recovered correlations with the *first* timepoint’s correlation matrix. The right panel compares the recovered correlations with the *last* timepoint’s correlation matrix. **d. Event-based correlations.** These datasets are each generated using five randomly drawn correlation matrices that each remain stable for a fifth of the total timecourse. The left panel displays the correlations between the recovered dynamic correlations and the underlying ground truth correlations. The right panels compare the recovered correlations with the correlation matrices unique to each event. The vertical lines denote event boundaries.

130 **Recovering dynamic higher-order correlations**

131 Following our approach to evaluating our ability to recover known dynamic first-order correlations from  
132 synthetic data, we generated an analogous second set of synthetic datasets that we designed to exhibit  
133 known dynamic first-order *and* second-order correlations (see *Synthetic data: simulating dynamic higher-order*  
134 *correlations*). We generated a total of ~~40–400~~ datasets that varied in how the first-order and second-order  
135 correlations changed over time. We then repeatedly applied Equation 4 using the overall best-performing  
136 kernel from our first-order tests (a Laplace kernel with a width of 20; Fig. 2) to assess how closely the  
137 recovered dynamic correlations matched the dynamic correlations we had embedded into the datasets.

138 Overall, we found that we could reliably recover both first-order and second-order correlations from  
139 the synthetic data (Fig. 3). When the correlations were stable for longer intervals, or changed gradually  
140 (constant, ramping, and event datasets), recovery performance was relatively high, and we were better able  
141 to recover dynamic first-order correlations than second-order correlations. ~~We expected that this would~~  
142 ~~happen, given that This is because~~ errors in our ~~estimation estimation~~ procedure at lower orders necessarily  
143 propagate to higher orders (since lower-order correlations are used to estimate higher-order correlations).  
144 ~~Interestingly, we also found that Conversely,~~ when the correlations were particularly *unstable* (random  
145 datasets), we better recovered second-order correlations. ~~This is because noises in our data generation~~  
146 ~~procedure propagates from higher orders to lower orders (see Synthetic data: simulating dynamic high-order~~  
147 ~~correlations).~~

148 ~~We also examined the impact of the data duration (Fig. S3) and complexity (number of zero-order features;~~  
149 ~~Fig. S4) on our ability to accurately recover ground truth first-order and second-order dynamic correlations.~~  
150 ~~In general, we found that our approach better recovers ground truth dynamic correlations from longer~~  
151 ~~duration timeseries data. We also found that our approach tends to best recover data generated using fewer~~  
152 ~~zero-order features (i.e., lower complexity), although this tendency was not strictly monotonic. Further,~~  
153 ~~because our data generation procedure requires  $O(K^4)$  memory to generate a second-order timeseries with  $K$~~   
154 ~~zero-order features, we were not able to fully explore how the number of zero-order features affects recovery~~  
155 ~~accuracy as the number of features gets larger (e.g., as it approaches the number of features present in the~~  
156 ~~fMRI data we examine below). Although we were not able to formally test this to our satisfaction, we expect~~  
157 ~~that accurately estimating dynamic high-order correlations would require data with many more zero-order~~  
158 ~~features than we were able to simulate. Our reasoning is that high-order correlations necessarily involve~~  
159 ~~larger numbers of lower-order features, so achieving adequate “resolution” high-order timeseries might~~  
160 ~~require many low-order features.~~

161 Taken together, our explorations using synthetic data indicated that we are able to partially, but not

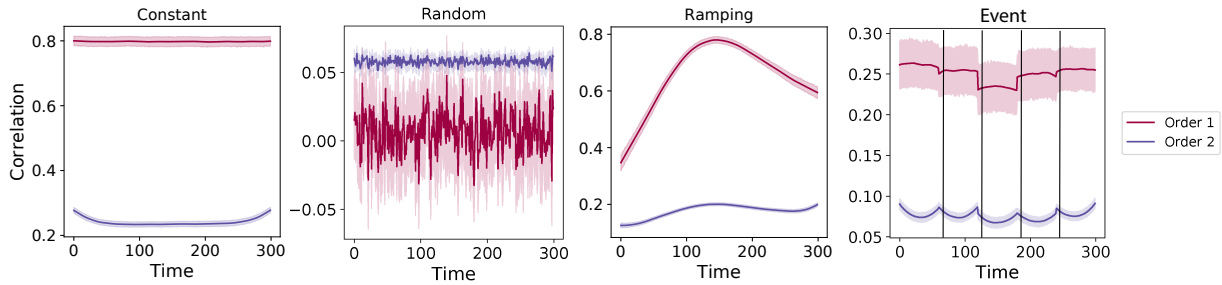


Figure 3: **Recovery of simulated first-order and second-order dynamic correlations.** Each panel displays the average correlations between the vectorized upper triangles of the recovered first-order and second-order correlation matrices and the true (simulated) first-order and second order correlation matrices at each timepoint and for each synthetic dataset. (The averages are taken across 10–100 different randomly generated synthetic datasets of the each given category, each with  $K = 10$  features and  $T = 300$  timepoints.) Error ribbons denote 95% confidence intervals (taken across datasets). For a complete description of each synthetic dataset, see *Synthetic data: simulating dynamic higher-order correlations*. All estimates represented in this figure were computed using a Laplace kernel (width = 20). **a. Constant correlations.** **Constant.** These datasets have stable (unchanging) underlying second-order correlation matrices. **b. Random correlations.** **Random.** These datasets are generated using a new independently drawn second-order correlation matrix at each timepoint. **c. Ramping correlations.** **Ramping.** These datasets are generated by smoothly varying the underlying second-order correlations between the randomly drawn correlation matrices at the first and last timepoints. **d. Event-based correlations.** **Event.** These datasets are each generated using five randomly drawn second-order correlation matrices that each remain stable for a fifth of the total timecourse. The vertical lines denote event boundaries. Note that the “dips” and “ramps” at the boundaries of sharp transitions (e.g., the beginning and ends of the “constant” and “ramping” datasets, and at the event boundaries of the “event” datasets) are finite-sample effects that reflect the reduced numbers of samples that may be used to accurately estimate correlations at sharp boundaries.

162 perfectly, recover ground truth dynamic first-order and second-order correlations. This suggests that our  
163 modeling approach provides a meaningful (if noisy) estimate of high-order correlations. We next turned  
164 to analyses of human fMRI data to examine whether the recovered dynamics might reflect the dynamics of  
165 human cognition during a naturalistic story-listening task.

## 166 Cognitively relevant dynamic high-order correlations in fMRI data

167 We used across-participant temporal decoders to identify cognitively relevant neural patterns in fMRI data  
168 (see *Forward inference and decoding accuracy*). The dataset we examined (collected by Simony et al., 2016)  
169 comprised four experimental conditions that exposed participants to stimuli that varied systematically in  
170 how cognitively engaging they were. The *intact* experimental condition had participants listen to an audio  
171 recording of a 10-minute story. The *paragraph*-scrambled experimental condition had participants listen to a  
172 temporally scrambled version of the story, where the paragraphs occurred out of order (but where the same  
173 total set of paragraphs were presented over the full listening interval). All participants in this condition  
174 experienced the scrambled paragraphs in the same order. The *word*-scrambled experimental condition had  
175 participants listen to a temporally scrambled version of the story where the words in the story occurred in a  
176 random order. All participants in the word condition experienced the scrambled words in the same order.  
177 Finally, in a *rest* experimental condition, participants lay in the scanner with no overt stimulus, with their  
178 eyes open (blinking as needed). This public dataset provided a convenient means of testing our hypothesis  
179 that different levels of cognitive processing and engagement are reflected in different orders of brain activity  
180 dynamics.

181 In brief, we computed timeseries of dynamic high-order correlations that were similar across participants  
182 in each of two randomly assigned groups: a training group and a test group. We then trained classifiers  
183 on the training group's data to match each sample from the test group with a stimulus timepoint. Each  
184 classifier comprised a weighted blend of neural patterns that reflected up to  $n^{\text{th}}$ -order dynamic correlations  
185 (see *Feature weighting and testing*, Fig. 10). We repeated this process for  $n \in \{0, 1, 2, \dots, 10\}$ . Our examinations  
186 of synthetic data suggested that none of the kernels we examined were “universal” in the sense of optimally  
187 recovering underlying correlations regardless of the temporal structure of those correlations. We found a  
188 similar pattern in the (real) fMRI data, whereby different kernels yielded different decoding accuracies, but  
189 no single kernel emerged as the clear “best.” In our analyses of neural data, we therefore averaged our  
190 decoding results over a variety of kernel shapes and widths in order to identify results that were robust to  
191 specific kernel parameters (see *Identifying robust decoding results*).

192 Our approach to estimating dynamic high-order correlations entails mapping the high-dimensional

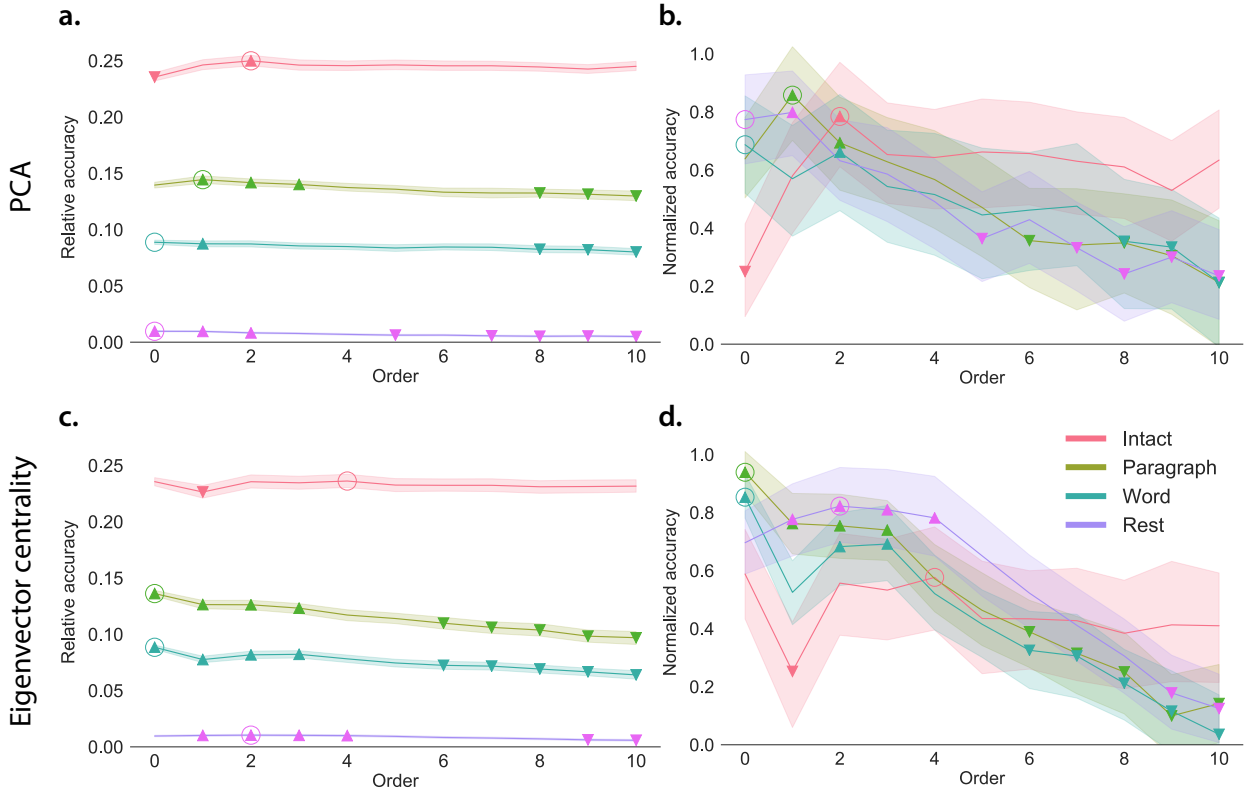


**Figure 4: Across-participant timepoint decoding accuracy varies with correlation order and cognitive engagement.** **a. Decoding accuracy as a function of order: PCA.** Order (x-axis) refers to the maximum order of dynamic correlations that were available to the classifiers (see *Feature weighting and testing*). The reported across-participant decoding accuracies are averaged over all kernel shapes and widths (see *Identifying robust decoding results*). The y-values are displayed relative to chance accuracy (intact:  $\frac{1}{300}$ ; paragraph:  $\frac{1}{272}$ ; word:  $\frac{1}{300}$ ; rest:  $\frac{1}{400}$ ; these chance accuracies were subtracted from the observed accuracies to obtain the relative accuracies reported on the y-axis). The error ribbons denote 95% confidence intervals across cross-validation folds (i.e., random assignments of participants to the training and test sets). The colors denote the experimental condition. Arrows denote sets of features that yielded reliably higher (upward facing) or lower (downward facing) decoding accuracy than the mean of all other features (via a two-tailed *t*-test, thresholded at  $p < 0.05$ ). Figure 5 displays additional comparisons between the decoding accuracies achieved using different sets of neural features. The circled values represent the maximum decoding accuracy within each experimental condition. **b. Normalized timepoint decoding accuracy as a function of order: PCA.** This panel displays the same results as Panel a, but here each curve has been normalized to have a maximum value of 1 and a minimum value of 0 (including the upper and lower bounds of the respective 95% confidence intervals). Panels a and b used PCA to project each high-dimensional pattern of dynamic correlations onto a lower-dimensional space. **c. Timepoint decoding accuracy as a function of order: eigenvector centrality.** This panel is in the same format as Panel a, but here eigenvector centrality has been used to project the high-dimensional patterns of dynamic correlations onto a lower-dimensional space. **d. Normalized timepoint decoding accuracy as a function of order: eigenvector centrality.** This panel is in the same format as Panel b, but here eigenvector centrality has been used to project the high-dimensional patterns of dynamic correlations onto a lower-dimensional space. See Figures S1 and S2 for decoding results broken down by kernel shape and width, respectively.

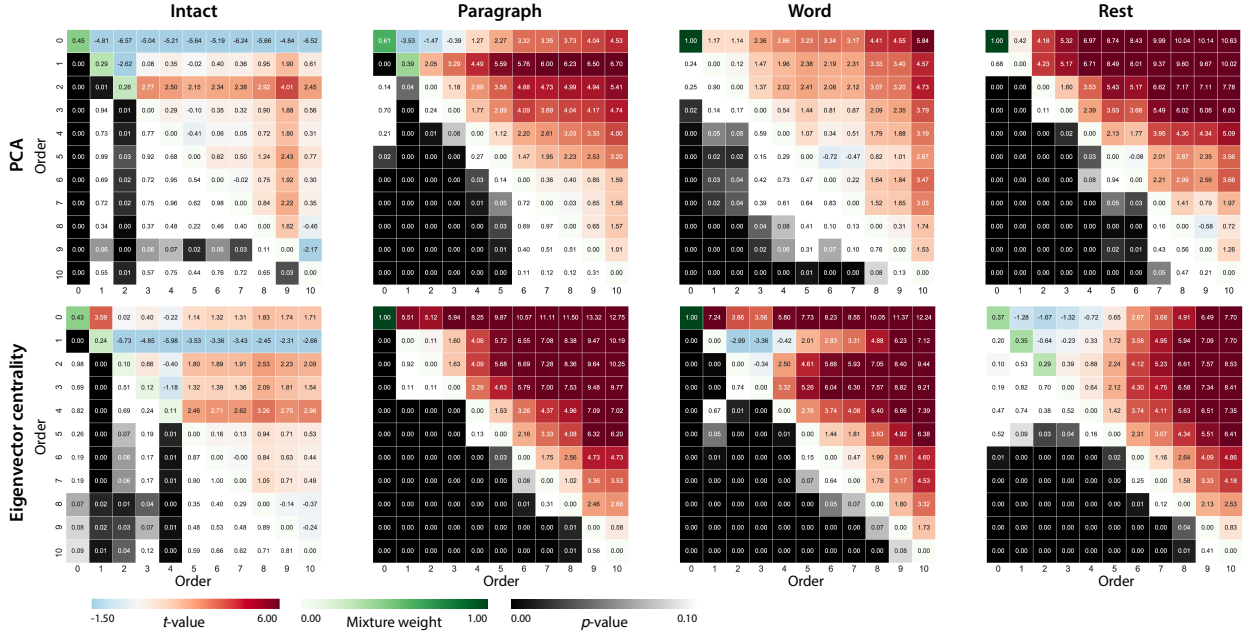


**Figure 5: Statistical summary of decoding accuracies for different neural features.** Each column of matrices displays decoding results for one experimental condition (intact, paragraph, word, and rest). We considered dynamic activity patterns (order 0) and dynamic correlations at different orders (order  $> 0$ ). We used two-tailed  $t$ -tests to compare the distributions of decoding accuracies obtained using each pair of features. The distributions for each feature reflect the set of average decoding accuracies (across all kernel parameters), obtained for each random assignment of training and test groups. In the upper triangles of each matrix, warmer colors (positive  $t$ -values) indicate that the neural feature indicated in the given row yielded higher accuracy than the feature indicated in the given column. Cooler colors (negative  $t$ -values) indicate that the feature in the given row yielded lower decoding accuracy than the feature in the given column. The lower triangles of each map denote the corresponding  $p$ -values for the  $t$ -tests. The diagonal entries display the relative average optimized weight given to each type of feature in a decoder that included all feature types (see *Feature weighting and testing*).

feature space of correlations (represented by a  $T$  by  $O(K^2)$  matrix) onto a lower-dimensional feature space (represented by a  $T$  by  $K$  matrix). We carried out two sets of analyses that differed in how this mapping was computed. The first set of analyses used PCA to find a low-dimensional embedding of the original dynamic correlation matrices (Fig. 4a,b). The second set of analyses characterized correlations in dynamics of each feature's eigenvector centrality, but did not preserve the underlying activity dynamics (Fig. 4c,d).

Both sets of temporal decoding analyses yielded qualitatively similar results for the auditory (non-rest) conditions of the experiment (Fig. 4: pink, green, and teal lines; Fig. 5: three leftmost columns). The highest decoding accuracy for participants who listened to the intact (unscrambled) story was achieved using high-order dynamic correlations (PCA: second-order; eigenvector-centrality: fourth-order). Scrambled versions of the story were best decoded by lower-order correlations (PCA/paragraph: first-order; PCA/word: order zero; eigenvector centrality/paragraph: order zero; eigenvector centrality/word: order zero). The two sets of analyses yielded different decoding results on resting state data (Fig. 4: purple lines; Fig. 5: rightmost

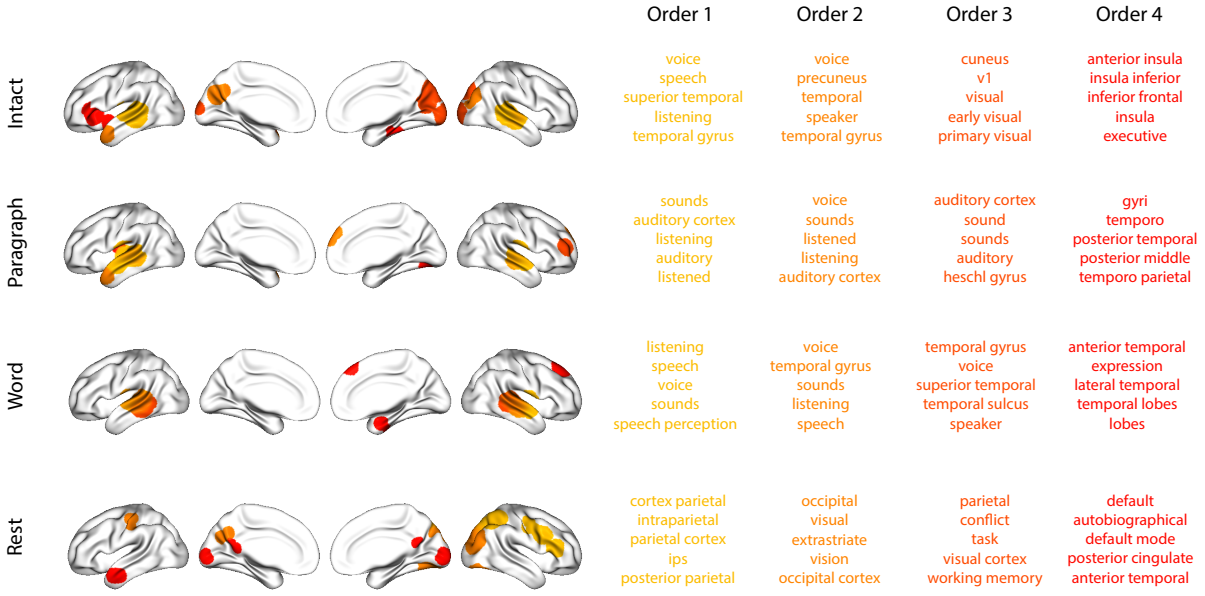


**Figure 6: Top terms associated with the most strongly correlated nodes at each order.** Each color corresponds to one order of inter-subject functional correlations. To calculate the dynamic correlations, eigenvector centrality has been used to project the high-dimensional patterns of dynamic correlations onto a lower-dimensional space at each previous order, which allows us to map the brain regions at each order by retaining the features of the original space. The inflated brain plots display the locations of the endpoints of the 10 strongest (absolute value) correlations at each order, thresholded at 0.999, and projected onto the cortical surface (Combrisson et al., 2019). The lists of terms on the right display the top five Neurosynth terms (Rubin et al., 2017) decoded from the corresponding brain maps for each order. Each row displays data from a different experimental condition. Additional maps and their corresponding Neurosynth terms may be found in the *Supplementary materials* (intact: Fig. S5; paragraph: Fig. S6; word: Fig. S7; rest: Fig. S8).

205 column). We note that, while the resting state times could be decoded reliably, the accuracies were only very  
 206 slightly above chance. We speculate that the decoders might have picked up on attentional drift, boredom,  
 207 or tiredness; we hypothesize that these all increased throughout the resting state scan. The decoders might  
 208 be picking up on aspects of these loosely defined cognitive states that are common across individuals. The  
 209 PCA-based approach achieved the highest resting state decoding accuracy using order zero features (non-  
 210 correlational, activation-based), whereas the eigenvector centrality-based approach achieved the highest  
 211 resting state decoding accuracy using second-order correlations. Taken together, these analyses indicate  
 212 that high-level cognitive processing (while listening to the intact story) is reflected in the dynamics of high-  
 213 order correlations in brain activity, whereas lower-level cognitive processing (while listening to scrambled  
 214 versions of the story that lack rich meaning) is reflected in the dynamics of lower-order correlations and  
 215 non-correlational activity dynamics. Further, these patterns are associated both with the underlying activity  
 216 patterns (characterized using PCA) and also with the changing relative positions that different brain areas  
 217 occupy in their associated networks (characterized using eigenvector centrality).

Having established that patterns of high-order correlations are informative to decoders, we next wondered which specific networks of brain regions contributed most to these patterns. As a representative example, we selected the kernel parameters that yielded decoding accuracies that were the most strongly correlated (across conditions and orders) with the average accuracies across all of the kernel parameters we examined. Using Figure 4c as a template, the best-matching kernel was a Laplace kernel with a width of 50 (Fig. 9d; also see Fig. S9). We used this kernel to compute a single  $K$  by  $K$   $n^{\text{th}}$ -order DISFC matrix for each experimental condition. We then used Neurosynth (Rubin et al., 2017) to compute the terms most highly associated with the most strongly correlated pairs of regions in each of these matrices (Fig. 6; see *Reverse inference*).

For all of the story listening conditions (intact, paragraph, and word; top three rows of Fig. 6), we found that first- and second-order correlations were most strongly associated with auditory and speech processing areas. During intact story listening, third-order correlations reflected integration with visual areas, and fourth-order correlations reflected integration with areas associated with high-level cognition and cognitive control, such as the ventrolateral prefrontal cortex. However, when participants listened to temporally scrambled stories, these higher-order correlations instead involved interactions with additional regions associated with speech and semantic processing (second and third rows of Fig. 6). By contrast, we found a much different set of patterns in the resting state data (Fig. 6, bottom row). First-order resting state correlations were most strongly associated with regions involved in counting and numerical understanding. Second-order resting state correlations were strongest in visual areas; third-order correlations were strongest in task-positive areas; and fourth-order correlations were strongest in regions associated with autobiographical and episodic memory. We carried out analogous analyses to create maps (and decode the top associated Neurosynth terms) for up to fifteenth-order correlations (Figs. S5, S6, S7, and S8). Of note, examining fifteenth-order correlations between 700 nodes using conventional methods would have required storing roughly  $\frac{700^{2 \times 15}}{2} \approx 1.13 \times 10^{85}$  floating point numbers—assuming single-precision (32 bits each), this would require roughly 32 times as many bits as there are molecules in the known universe! Although these fifteenth-order correlations do appear (visually) to have some well-formed structure, we provide this latter example primarily as a demonstration of the efficiency and scalability of our approach.

## Discussion

We tested the hypothesis that high-level cognition is reflected in high-order brain network dynamics (e.g., see Reimann et al., 2017; Solomon et al., 2019). We examined high-order network dynamics in functional neuroimaging data collected during a story listening experiment. When participants listened to an auditory

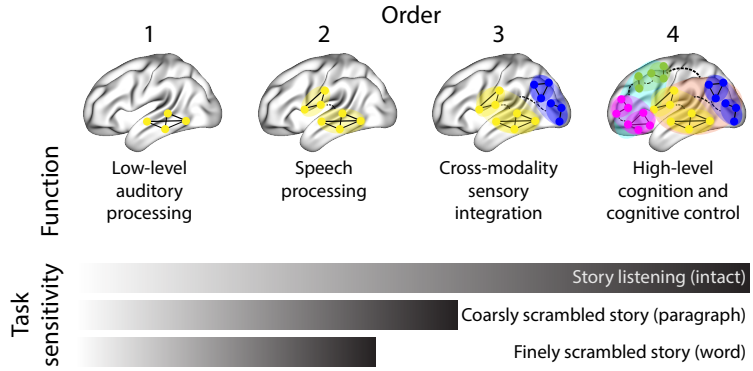


**Figure 7: Proposed high-order network dynamics underlying high-level cognition during story listening.** Schematic depicts higher orders of network interactions supporting higher-level aspects of cognitive processing. When tasks evoke richer, deeper, and/or higher-level processing, this is reflected in higher-order network interactions.

recording of the story, participants exhibited similar high-order brain network dynamics. By contrast, when participants instead listened to temporally scrambled recordings of the story, only lower-order brain network dynamics were similar across participants. Our results indicate that higher orders of network interactions support higher-level aspects of cognitive processing (Fig. 7).

The notion that cognition is reflected in (and possibly mediated by) patterns of first-order network dynamics has been suggested by or proposed in myriad empirical studies and reviews (e.g., Bressler & Kelso, 2001; Chang & Glover, 2010; Demertzi et al., 2019; Fong et al., 2019; Gonzalez-Castillo et al., 2019; Liégeois et al., 2019; Lurie et al., 2018; Manning et al., 2018; McIntosh, 2000; Park et al., 2018; Preti et al., 2017; Roy et al., 2019; Turk-Browne, 2013; Zou et al., 2019). Our study extends this line of work by finding cognitively relevant *higher-order* network dynamics that reflect ongoing cognition. Our findings also complement other work that uses graph theory and topology to characterize how brain networks reconfigure during cognition (e.g., Bassett et al., 2006; Betzel et al., 2019; McIntosh & Jirsa, 2019; Reimann et al., 2017; Sizemore et al., 2018; Toker & Sommer, 2019; Zheng et al., 2019).

An open question not addressed by our study pertains to how different structures integrate incoming information with different time constants. For example, one line of work suggests that the cortical surface comprises a structured map such that nearby brain structures process incoming information at similar timescales. Low-level sensory areas integrate information relatively quickly, whereas higher-level regions integrate information relatively slowly (Baldassano et al., 2017; Chien & Honey, 2019; Hasson et al., 2015, 2008; Honey et al., 2012; Lerner et al., 2014, 2011). A similar hierarchy appears to play a role in predicting future events (C. S. Lee et al., 2020). Other related work in human and mouse brains indicates that the temporal response profile of a given brain structure may relate to how strongly connected that structure is with other brain areas (Fallon et al., 2020). Further study is needed to understand the role of

271 temporal integration at different scales of network interaction, and across different anatomical structures.  
272 Importantly, our analyses do not speak to the physiological basis of higher-order dynamics, and could  
273 reflect nonlinearities, chaotic patterns, non-stationarities, and/or multistability, etc. However, our decoding  
274 analyses do indicate that higher-order dynamics are consistent across individuals, and therefore unlikely to  
275 reflect non-stimulus-driven dynamics that are unlikely to be similar across individuals.

276 One limitation of our approach relates to how noise propagates in our estimation procedure. Specifically,  
277 our procedure for estimating high-order dynamic correlations depends on estimates of lower-order dynamic  
278 correlations. This means that our measures of which higher-order patterns are reliable and stable across  
279 experimental conditions are partially confounded with the stability of lower-order patterns. Prior work  
280 suggests that the stability of what we refer to here as first-order dynamics likely varies across the experimental  
281 conditions we examined (Simony et al., 2016). Therefore a caveat to our claim that richer stimuli evoke more  
282 stable higher-order dynamics is that our approach assumes that those high-order dynamics reflect relations  
283 or interactions between lower-order features.

284 Another potential limitation of our approach relates to recent work suggesting that the brain undergoes  
285 rapid state changes, for example across event boundaries (e.g., Baldassano et al., 2017). Shappell et al.  
286 (2019) used hidden semi-Markov models to estimate state-specific network dynamics (also see Vidaurre et  
287 al., 2018). Our general approach might be extended by considering putative state transitions. For example,  
288 rather than weighting all timepoints using a similar kernel (Eqn. 4), the kernel function could adapt on a  
289 timepoint-by-timepoint basis such that only timepoints determined to be in the same “state” were given  
290 non-zero weight.

291 Identifying high-order network dynamics associated with high-level cognition required several impor-  
292 tant methods advances. First, we used kernel-based dynamic correlations to extended the notion of (static)  
293 inter-subject functional connectivity (Simony et al., 2016) to a dynamic measure of inter-subject functional  
294 connectivity (DISFC) that does not rely on sliding windows (e.g., as in Manning et al., 2018), and that may  
295 be computed at individual timepoints. This allowed us to precisely characterize stimulus-evoked network  
296 dynamics that were similar across individuals. Second, we developed a computational framework for  
297 efficiently and scalably estimating high-order dynamic correlations. Our approach uses dimensionality  
298 reduction algorithms and graph measures to obtain low-dimensional embeddings of patterns of network  
299 dynamics. Third, we developed an analysis framework for identifying robust decoding results by carrying  
300 out our analyses using a range of parameter values and identifying which results were robust to specific  
301 parameter choices. By showing that high-level cognition is reflected in high-order network dynamics, we  
302 have elucidated the next step on the path towards understanding the neural basis of cognition.

303 **Methods**

304 Our general approach to efficiently estimating high-order dynamic correlations comprises four general  
305 steps (Fig. 8). First, we derive a kernel-based approach to computing dynamic pairwise correlations in  
306 a  $T$  (timepoints) by  $K$  (features) multivariate timeseries,  $\mathbf{X}_0$ . This yields a  $T$  by  $O(K^2)$  matrix of dynamic  
307 correlations,  $\mathbf{Y}_1$ , where each row comprises the upper triangle and diagonal of the correlation matrix at  
308 a single timepoint, reshaped into a row vector (this reshaped vector is  $(\frac{K^2-K}{2} + K)$ -dimensional). Second,  
309 we apply a dimensionality reduction step to project the matrix of dynamic correlations back onto a  $K$ -  
310 dimensional space. This yields a  $T$  by  $K$  matrix,  $\mathbf{X}_1$ , that reflects an approximation of the dynamic correlations  
311 reflected in the original data. Third, we use repeated applications of the kernel-based dynamic correlation  
312 step to  $\mathbf{X}_n$  and the dimensionality reduction step to the resulting  $\mathbf{Y}_{n+1}$  to estimate high-order dynamic  
313 correlations. Each application of these steps to a  $T$  by  $K$  time series  $\mathbf{X}_n$  yields a  $T$  by  $K$  matrix,  $\mathbf{X}_{n+1}$ , that  
314 reflects the dynamic correlations between the columns of  $\mathbf{X}_n$ . In this way, we refer to  $n$  as the *order* of the  
315 timeseries, where  $\mathbf{X}_0$  (order 0) denotes the original data and  $\mathbf{X}_n$  denotes (approximated)  $n^{\text{th}}$ -order dynamic  
316 correlations between the columns of  $\mathbf{X}_0$ . Finally, we use a cross-validation-based decoding approach to  
317 evaluate how well information contained in a given order (or weighted mixture of orders) may be used  
318 to decode relevant cognitive states. If including a given  $\mathbf{X}_n$  in the feature set yields higher classification  
319 accuracy on held-out data, we interpret this as evidence that the given cognitive states are reflected in  
320 patterns of  $n^{\text{th}}$ -order correlations.

321 All of the code used to produce the figures and results in this manuscript, along with links to the  
322 corresponding datasets, may be found at [github.com/ContextLab/timecorr-paper](https://github.com/ContextLab/timecorr-paper). In addition, we have  
323 released a Python toolbox for computing dynamic high-order correlations in timeseries data; our toolbox  
324 may be found at [timecorr.readthedocs.io](https://timecorr.readthedocs.io).

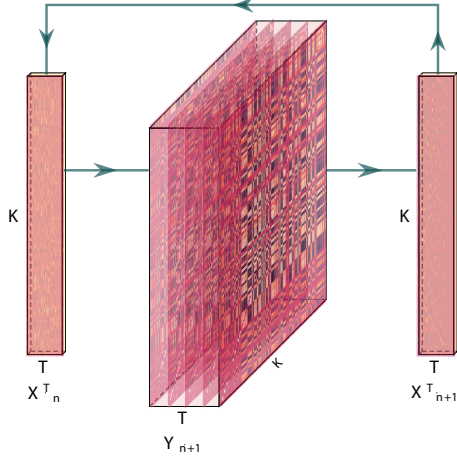


Figure 8: **Estimating dynamic high-order correlations.** Given a  $T$  by  $K$  matrix of multivariate timeseries data,  $\mathbf{X}_n$  (where  $n \in \mathbb{N}, n \geq 0$ ), we use Equation 4 to compute a timeseries of  $K$  by  $K$  correlation matrices,  $\mathbf{Y}_{n+1}$ . We then approximate  $\mathbf{Y}_{n+1}$  with the  $T$  by  $K$  matrix  $\mathbf{X}_{n+1}$ . This process may be repeated to scalably estimate iteratively higher-order correlations in the data. Note that the transposes of  $\mathbf{X}_n$  and  $\mathbf{X}_{n+1}$  are displayed in the figure for compactness.

### 325 Kernel-based approach for computing dynamic correlations

Given a  $T$  by  $K$  matrix of observations,  $\mathbf{X}$ , we can compute the (static) Pearson's correlation between any pair of columns,  $\mathbf{X}(\cdot, i)$  and  $\mathbf{X}(\cdot, j)$  using (Pearson, 1901):

$$\text{corr}(\mathbf{X}(\cdot, i), \mathbf{X}(\cdot, j)) = \frac{\sum_{t=1}^T (\mathbf{X}(t, i) - \bar{\mathbf{X}}(\cdot, i))(\mathbf{X}(t, j) - \bar{\mathbf{X}}(\cdot, j))}{\sqrt{\sum_{t=1}^T \sigma_{\mathbf{X}(\cdot, i)}^2 \sigma_{\mathbf{X}(\cdot, j)}^2}}, \text{ where} \quad (1)$$

$$\bar{\mathbf{X}}(\cdot, k) = \frac{1}{T} \sum_{t=1}^T \mathbf{X}(t, k), \text{ and} \quad (2)$$

$$\sigma_{\mathbf{X}(\cdot, k)}^2 = \frac{1}{T} \sum_{t=1}^T (\mathbf{X}(t, k) - \bar{\mathbf{X}}(\cdot, k))^2 \quad (3)$$

- 326 We can generalize this formula to compute time-varying correlations by incorporating a *kernel function* that  
 327 takes a time  $t$  as input, and returns how much the observed data at each timepoint  $\tau \in [-\infty, \infty]$  contributes  
 328 to the estimated instantaneous correlation at time  $t$  (Fig. 9; also see Allen et al., 2012, for a similar approach).

329

Given a kernel function  $\kappa_t(\cdot)$  for timepoint  $t$ , evaluated at timepoints  $\tau \in [1, \dots, T]$ , we can update the

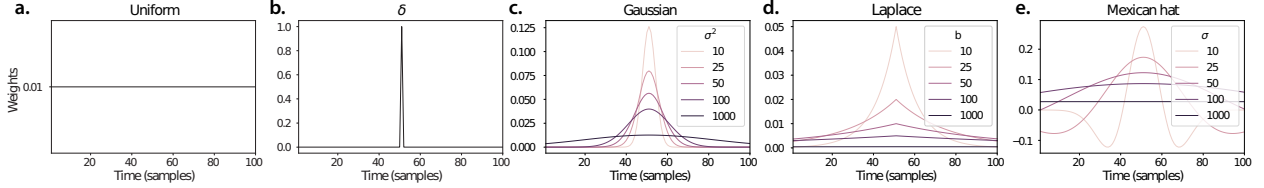


**Figure 9: Examples of kernel functions.** Each panel displays per-timepoint weights for a kernel centered at  $t = 50$ , evaluated at 100 timepoints ( $\tau \in [1, \dots, 100]$ ). **a. Uniform kernel.** The weights are timepoint-invariant; observations at all timepoints are weighted equally, and do not change as a function of  $\tau$ . This is a special case kernel function that reduces dynamic correlations to static correlations. **b. Dirac  $\delta$  kernel.** Only the observation at timepoint  $t$  is given a non-zero weight (of 1). **c. Gaussian kernels.** Each kernel's weights fall off in time according to a Gaussian probability density function centered on time  $t$ . Weights derived using several different example width parameters ( $\sigma^2$ ) are displayed. **d. Laplace kernels.** Each kernel's weights fall off in time according to a Laplace probability density function centered on time  $t$ . Weights derived using several different example width parameters ( $b$ ) are displayed. **e. Mexican hat (Ricker wavelet) kernels.** Each kernel's weights fall off in time according to a Ricker wavelet centered on time  $t$ . This function highlights the *contrasts* between local versus surrounding activity patterns in estimating dynamic correlations. Weights derived using several different example width parameters ( $\sigma$ ) are displayed.

static correlation formula in Equation 1 to estimate the *instantaneous correlation* at timepoint  $t$ :

$$\text{timecorr}_{\kappa_t}(\mathbf{X}(\cdot, i), \mathbf{X}(\cdot, j)) = \frac{\sum_{\tau=1}^T (\mathbf{X}(\tau, i) - \tilde{\mathbf{X}}_{\kappa_t}(\cdot, i))(\mathbf{X}(\tau, j) - \tilde{\mathbf{X}}_{\kappa_t}(\cdot, j))}{\sqrt{\sum_{\tau=1}^T \tilde{\sigma}_{\kappa_t}^2(\mathbf{X}(\cdot, i))\tilde{\sigma}_{\kappa_t}^2(\mathbf{X}(\cdot, j))}}, \text{ where} \quad (4)$$

$$\tilde{\mathbf{X}}_{\kappa_t}(\cdot, k) = \sum_{\tau=1}^T \kappa_t(\tau) \mathbf{X}(\tau, k), \quad (5)$$

$$\tilde{\sigma}_{\kappa_t}^2(\mathbf{X}(\cdot, k)) = \sum_{\tau=1}^T (\mathbf{X}(\tau, k) - \tilde{\mathbf{X}}_{\kappa_t}(\cdot, k))^2. \quad (6)$$

330 Here  $\text{timecorr}_{\kappa_t}(\mathbf{X}(\cdot, i), \mathbf{X}(\cdot, j))$  reflects the correlation at time  $t$  between columns  $i$  and  $j$  of  $\mathbf{X}$ , estimated using  
 331 the kernel  $\kappa_t$ . We evaluate Equation 4 in turn for each pair of columns in  $\mathbf{X}$  and for kernels centered on each  
 332 timepoint in the timeseries, respectively, to obtain a  $T$  by  $K$  by  $K$  timeseries of dynamic correlations,  $\mathbf{Y}$ . For  
 333 convenience, we then reshape the upper triangles and diagonals of each timepoint's symmetric correlation  
 334 matrix into a row vector to obtain an equivalent  $T$  by  $\left(\frac{K^2-K}{2} + K\right)$  matrix.

### 335 Dynamic inter-subject functional connectivity (DISFC)

Equation 4 provides a means of taking a single observation matrix,  $\mathbf{X}_n$  and estimating the dynamic correlations from moment to moment,  $\mathbf{Y}_{n+1}$ . Suppose that one has access to a set of multiple observation matrices that reflect the same phenomenon. For example, one might collect neuroimaging data from several experimental participants, as each participant performs the same task (or sequence of tasks). Let  $\mathbf{X}_n^1, \mathbf{X}_n^2, \dots, \mathbf{X}_n^P$  reflect the  $T$  by  $K$  observation matrices ( $n = 0$ ) or reduced correlation matrices ( $n > 0$ ) for each of  $P$

participants in an experiment. We can use *inter-subject functional connectivity* (ISFC; Simony & Chang, 2020; Simony et al., 2016) to compute the stimulus-driven correlations reflected in the multi-participant dataset at a given timepoint  $t$  using:

$$\bar{\mathbf{C}}(t) = M \left( R \left( \frac{1}{2P} \sum_{p=1}^P Z(\mathbf{Y}_{n+1}^p(t))^\top + Z(\mathbf{Y}_{n+1}^p(t)) \right) \right), \quad (7)$$

where  $M$  extracts and vectorizes the upper triangle and diagonal of a symmetric matrix,  $Z$  is the Fisher  $z$ -transformation (Zar, 2010):

$$Z(r) = \frac{\log(1+r) - \log(1-r)}{2}, \quad (8)$$

$R$  is the inverse of  $Z$ :

$$R(z) = \frac{\exp(2z-1)}{\exp(2z+1)}, \quad (9)$$

and  $\mathbf{Y}_{n+1}^p(t)$  denotes the correlation matrix at timepoint  $t$  (Eqn. 4) between each column of  $\mathbf{X}_n^p$  and each column of the average  $\mathbf{X}_n$  from all *other* participants,  $\bar{\mathbf{X}}_n^p$ :

$$\bar{\mathbf{X}}_n^p = \frac{1}{P-1} \sum_{q \in \setminus p} \mathbf{X}_n^q, \quad (10)$$

336 where  $\setminus p$  denotes the set of all participants other than participant  $p$ . In this way, the  $T$  by  $(\frac{K^2-K}{2} + K)$  DISFC  
337 matrix  $\bar{\mathbf{C}}$  provides a time-varying extension of the ISFC approach developed by Simony et al. (2016).

### 338 Low-dimensional representations of dynamic correlations

339 Given a  $T$  by  $(\frac{K^2-K}{2} + K)$  matrix of  $n^{\text{th}}$ -order dynamic correlations,  $\mathbf{Y}_n$ , we propose two general approaches  
340 to computing a  $T$  by  $K$  low-dimensional representation of those correlations,  $\mathbf{X}_n$ . The first approach uses  
341 dimensionality reduction algorithms to project  $\mathbf{Y}_n$  onto a  $K$ -dimensional space. The second approach uses  
342 graph measures to characterize the relative positions of each feature ( $k \in [1, \dots, K]$ ) in the network defined  
343 by the correlation matrix at each timepoint.

#### 344 Dimensionality reduction-based approaches to computing $\mathbf{X}_n$

345 The modern toolkit of dimensionality reduction algorithms include Principal Components Analysis (PCA;  
346 Pearson, 1901), Probabilistic PCA (PPCA; Tipping & Bishop, 1999), Exploratory Factor Analysis (EFA;

347 Spearman, 1904), Independent Components Analysis (ICA; Comon et al., 1991; Jutten & Herault, 1991),  
348 *t*-Stochastic Neighbor Embedding (*t*-SNE; van der Maaten & Hinton, 2008), Uniform Manifold Approximation  
349 and Projection (UMAP; McInnes et al., 2018), non-negative matrix factorization (NMF; D. D. Lee  
350 & Seung, 1999), Topographic Factor Analysis (TFA; Manning et al., 2014), Hierarchical Topographic Factor  
351 analysis (HTFA; Manning et al., 2018), Topographic Latent Source Analysis (TLSA; Gershman et al.,  
352 2011), dictionary learning (J. Mairal et al., 2009; J. B. Mairal et al., 2009), and deep auto-encoders (Hinton  
353 & Salakhutdinov, 2006), among others. While complete characterizations of each of these algorithms is  
354 beyond the scope of the present manuscript, the general intuition driving these approaches is to compute  
355 the  $T$  by  $K$  matrix,  $\mathbf{X}$ , that is closest to the original  $T$  by  $J$  matrix,  $\mathbf{Y}$ , where (typically)  $K \ll J$ . The different  
356 approaches place different constraints on what properties  $\mathbf{X}$  must satisfy and which aspects of the data are  
357 compared (and how) in order to optimize how well  $\mathbf{X}$  approximates  $\mathbf{Y}$ .

358 Applying dimensionality reduction algorithms to  $\mathbf{Y}$  yields an  $\mathbf{X}$  whose columns reflect weighted combi-  
359 nations (or nonlinear transformations) of the original columns of  $\mathbf{Y}$ . This has two main consequences. First,  
360 with each repeated dimensionality reduction, the resulting  $\mathbf{X}_n$  has lower and lower fidelity (with respect to  
361 what the “true”  $\mathbf{Y}_n$  might have looked like without using dimensionality reduction to maintain tractability).  
362 In other words, computing  $\mathbf{X}_n$  is a lossy operation. Second, whereas each column of  $\mathbf{Y}_n$  may be mapped  
363 directly onto specific pairs of columns of  $\mathbf{X}_{n-1}$ , the columns of  $\mathbf{X}_n$  reflect weighted combinations and/or  
364 nonlinear transformations of the columns of  $\mathbf{Y}_n$ . Many dimensionality reduction algorithms are invertible  
365 (or approximately invertible). However, attempting to map a given  $\mathbf{X}_n$  back onto the original feature space  
366 of  $\mathbf{X}_0$  will usually require  $O(TK^2)$  space and therefore becomes intractable as  $n$  or  $K$  grow large.

### 367 **Graph measure approaches to computing $\mathbf{X}_n$**

368 The above dimensionality reduction approaches to approximating a given  $\mathbf{Y}_n$  with a lower-dimensional  
369  $\mathbf{X}_n$  preserve a (potentially recombined and transformed) mapping back to the original data in  $\mathbf{X}_0$ . We also  
370 explore graph measures that instead characterize each feature’s relative *position* in the broader network of  
371 interactions and connections. To illustrate the distinction between the two general approaches we explore,  
372 suppose a network comprises nodes  $A$  and  $B$ , along with several other nodes. If  $A$  and  $B$  exhibit uncorrelated  
373 activity patterns, then by definition the functional connection (correlation) between them will be close to  
374 0. However, if  $A$  and  $B$  each interact with *other* nodes in similar ways, we might attempt to capture those  
375 similarities between  $A$ ’s and  $B$ ’s interactions with those other members of the network.

376 In general, graph measures take as input a matrix of interactions (e.g., using the above notation, a  $K$   
377 by  $K$  correlation matrix or binarized correlation matrix reconstituted from a single timepoint’s row of  $\mathbf{Y}$ ),

378 and return as output a set of  $K$  measures describing how each node (feature) sits within that correlation  
379 matrix with respect to the rest of the population. Widely used measures include betweenness centrality (the  
380 proportion of shortest paths between each pair of nodes in the population that involves the given node  
381 in question; e.g., Barthélemy, 2004; Freeman, 1977; Geisberger et al., 2008; Newman, 2005; Opsahl et al.,  
382 2010); diversity and dissimilarity (characterizations of how differently connected a given node is from others  
383 in the population; e.g., Lin, 2009; Rao, 1982; Ricotta & Szeidl, 2006); eigenvector centrality and pagerank  
384 centrality (measures of how influential a given node is within the broader network; e.g., Bonacich, 2007;  
385 Halu et al., 2013; Lohmann et al., 2010; Newman, 2008); transfer entropy and flow coefficients (a measure of  
386 how much information is flowing from a given node to other nodes in the network; e.g., Honey et al., 2007;  
387 Schreiber, 2000);  $k$ -coreness centrality (a measure of the connectivity of a node within its local subgraph; e.g.,  
388 Alvarez-Hamelin et al., 2005; Christakis & Fowler, 2010); within-module degree (a measure of how many  
389 connections a node has to its close neighbors in the network; e.g., Rubinov & Sporns, 2010); participation  
390 coefficient (a measure of the diversity of a node's connections to different subgraphs in the network; e.g.,  
391 Rubinov & Sporns, 2010); and subgraph centrality (a measure of a node's participation in all of the network's  
392 subgraphs; e.g., Estrada & Rodríguez-Velázquez, 2005); among others.

393 For a given graph measure,  $\eta : \mathbb{R}^{K \times K} \rightarrow \mathbb{R}^K$ , we can use  $\eta$  to transform each row of  $\mathbf{Y}_n$  in a way that  
394 characterizes the corresponding graph properties of each column. This results in a new  $T$  by  $K$  matrix,  
395  $\mathbf{X}_n$ , that reflects how the features reflected in the columns of  $\mathbf{X}_{n-1}$  participate in the network during each  
396 timepoint (row).

## 397 Dynamic higher-order correlations

398 Because  $\mathbf{X}_n$  has the same shape as the original data  $\mathbf{X}_0$ , approximating  $\mathbf{Y}_n$  with a lower-dimensional  $\mathbf{X}_n$   
399 enables us to estimate high-order dynamic correlations in a scalable way. Given a  $T$  by  $K$  input matrix, the  
400 output of Equation 4 requires  $O(TK^2)$  space to store. Repeated applications of Equation 4 (i.e., computing  
401 dynamic correlations between the columns of the outputted dynamic correlation matrix) each require  
402 exponentially more space; in general the  $n^{\text{th}}$ -order dynamic correlations of a  $T$  by  $K$  timeseries occupies  
403  $O(TK^{2^n})$  space. However, when we approximate or summarize the output of Equation 4 with a  $T$  by  $K$  matrix  
404 (as described above), it becomes feasible to compute even very high-order correlations in high-dimensional  
405 data. Specifically, approximating the  $n^{\text{th}}$ -order dynamic correlations of a  $T$  by  $K$  timeseries requires only  
406  $O(TK^2)$  additional space— the same as would be required to compute first-order dynamic correlations. In  
407 other words, the space required to store  $n + 1$  multivariate timeseries reflecting up to  $n^{\text{th}}$  order correlations  
408 in the original data scales linearly with  $n$  using our approach (Fig. 8).

409 **Data**

410 We examined two types of data: synthetic data and human functional neuroimaging data. We constructed  
411 and leveraged the synthetic data to evaluate our general approach (for a related validation approach see  
412 Thompson et al., 2018). Specifically, we tested how well Equation 4 could be used to recover known dynamic  
413 correlations using different choices of kernel ( $\kappa$ ; Fig. 9), for each of several synthetic datasets that exhibited  
414 different temporal properties. We also simulated higher-order correlations and tested how well Equation 4  
415 could recover these correlations using the best kernel from the previous synthetic data analyses. We then  
416 applied our approach to a functional neuroimaging dataset to test the hypothesis that ongoing cognitive  
417 processing is reflected in high-order dynamic correlations. We used an across-participant classification test  
418 to estimate whether dynamic correlations of different orders contain information about which timepoint in  
419 a story participants were listening to.

420 **Synthetic data: simulating dynamic first-order correlations**

421 We constructed a total of ~~40-400~~ different multivariate timeseries, collectively reflecting a total of 4 qual-  
422 itatively different patterns of dynamic first-order correlations (i.e., ~~10-100~~ datasets reflecting each type of  
423 dynamic pattern). Each timeseries comprised 50 features (dimensions) that varied over 300 timepoints. The  
424 observations at each timepoint were drawn from a zero-mean multivariate Gaussian distribution with a co-  
425 variance matrix defined for each timepoint as described below. We drew the observations at each timepoint  
426 independently from the draws at all other timepoints; in other words, for each observation  $s_t \sim \mathcal{N}(\mathbf{0}, \Sigma_t)$  at  
427 timepoint  $t$ ,  $p(s_t) = p(s_t | s_{\setminus t})$ .

**Constant.** We generated data with stable underlying correlations to evaluate how Equation 4 characterized correlation “dynamics” when the ground truth correlations were static. We constructed ~~10-100~~ multivariate timeseries whose observations were each drawn from a single (stable) Gaussian distribution. For each dataset (indexed by  $m$ ), we constructed a random covariance matrix,  $\Sigma_m$ :

$$\Sigma_m = \mathbf{C}\mathbf{C}^\top, \text{ where} \quad (11)$$

$$\mathbf{C}(i, j) \sim \mathcal{N}(0, 1), \text{ and where} \quad (12)$$

428  $i, j \in [1, 2, \dots, 50]$ . In other words, all of the observations (for each of the 300 timepoints) within each dataset  
429 were drawn from a multivariate Gaussian distribution with the same covariance matrix, and the ~~10-100~~  
430 datasets each used a different covariance matrix.

431 **Random.** We generated a second set of 10–100 synthetic datasets whose observations at each timepoint were  
 432 drawn from a Gaussian distribution with a new randomly constructed (using Eqn. 11) covariance matrix.  
 433 Because each timepoint’s covariance matrix was drawn independently from the covariance matrices for all  
 434 other timepoints, these datasets provided a test of reconstruction accuracy in the absence of any meaningful  
 435 underlying temporal structure in the dynamic correlations underlying the data.

**Ramping.** We generated a third set of 10–100 synthetic datasets whose underlying correlations changed gradually over time. For each dataset, we constructed two *anchor* covariance matrices using Equation 11,  $\Sigma_{\text{start}}$  and  $\Sigma_{\text{end}}$ . For each of the 300 timepoints in each dataset, we drew the observations from a multivariate Gaussian distribution whose covariance matrix at each timepoint  $t \in [0, \dots, 299]$  was given by

$$\Sigma_t = \left(1 - \frac{t}{299}\right)\Sigma_{\text{start}} + \frac{t}{299}\Sigma_{\text{end}}. \quad (13)$$

436 The gradually changing correlations underlying these datasets allow us to evaluate the recovery of dynamic  
 437 correlations when each timepoint’s correlation matrix is unique (as in the random datasets), but where the  
 438 correlation dynamics are structured and exhibit first-order autocorrelations (as in the constant datasets).

439 **Event.** We generated a fourth set of 10–100 synthetic datasets whose underlying correlation matrices  
 440 exhibited prolonged intervals of stability, interspersed with abrupt changes. For each dataset, we used  
 441 Equation 11 to generate 5 random covariance matrices. We constructed a timeseries where each set of  
 442 60 consecutive samples was drawn from a Gaussian with the same covariance matrix. These datasets  
 443 were intended to simulate a system that exhibits periods of stability punctuated by occasional abrupt state  
 444 changes.

#### 445 Synthetic data: simulating dynamic high-order correlations

446 We developed an iterative procedure for constructing timeseries data that exhibits known dynamic high-  
 447 order correlations. The procedure builds on our approach to generating dynamic first-order correlations.  
 448 Essentially, once we generate a timeseries with known first-order correlations, we can use the known first-  
 449 order correlations as a template to generate a new timeseries of second-order correlations. In turn, we can  
 450 generate a timeseries of third-order correlations from the second-order correlations, and so on. In general,  
 451 we can generate order  $n$  correlations given a timeseries of order  $n - 1$  correlations, for any  $n > 1$ . Finally,  
 452 given the order  $n$  timeseries, we can reverse the preceding process to generate an order  $n - 1$  timeseries, an  
 453 order  $n - 2$  order timeseries, and so on, until we obtain an order 0 timeseries of simulated data that reflects

454 the chosen high-order dynamics.

The central mathematical ~~operations~~ operation in our procedure ~~are two bookkeeping functions, `vec()` and `mat()`. The `vec()` function takes as input~~ is the Kronecker product ( $\otimes$ ). The Kronecker product of a  $K \times K$  symmetric matrix and returns as output a  $(\frac{K^2-K}{2} + K)$ -dimensional column vector containing matrix,  $m_1$ , with itself (i.e.,  $m_1 \otimes m_1$ ) produces a new  $K^2 \times K^2$  matrix,  $m_2$  whose entries reflect a scaled tiling of the entries in the upper triangle and diagonal. The `mat()` function inverts `vec()` by taking as input a  $(\frac{K^2-K}{2} + K)$ -dimensional column vector and returning a  $K \times K$  symmetric matrix as output. We can then generate an order  $m_1$ . If these tilings (scaled copies of  $m_1$ ) are indexed by row and column, then the tile in the  $i^{\text{th}}$  row and  $j^{\text{th}}$  column contains the entries of  $m_1$ , multiplied by  $m_1(i, j)$ . Following this pattern, the Kronecker product  $m_2 \otimes m_2$  yields the  $K^4 \times K^4$  matrix  $m_3$  whose tiles are scaled copies of  $m_2$ . In general, repeated applications of the Kronecker self-product may be used to generate  $m_{n+1} = m_n \otimes m_n$  for  $n > 1$ , where  $m_{n+1}$  is a  $K^{2^n} \times K^{2^n}$  matrix. After generating a first-order timeseries of dynamic correlations (see *Synthetic data: simulating dynamic first-order correlations*), we use this procedure (applied independently at each timepoint) to transform it into a timeseries of  $n$  correlation matrices (for one timepoint,  $t$ ) from an order  $n - 1$  template (from the same timepoint) as follows:

$$\Sigma_n(t) = \text{mat}(\text{vec}(\Sigma_{n-1}(t)) \otimes \text{vec}(\Sigma_{n-1}(t))^\top).$$

455  $n^{\text{th}}$ -order correlations. When  $m_{n+1}$  is generated in this way, the temporal structure of the full timeseries (i.e.,  
456 constant, random, ramping, event) is preserved, since changes in the original first-order timeseries are also  
457 reflected in the scaled tilings of itself that comprise the higher-order matrices.

Given a timeseries of ~~order- $n$  correlation matrices, we can draw~~  $n^{\text{th}}$ -order correlations, we then need to work “backwards” in order to generate the order-zero timeseries. If the  $n^{\text{th}}$ -order correlation matrix at a given timepoint is  $m_n$ , then we can generate an order  $n - 1$  correlation matrix ~~for each timepoint  $t$  using~~

$$\sigma_{n-1}(t) \sim \mathcal{N}(0, \Sigma_n(t))$$

$$\Sigma_{n-1}(t) = \text{mat}(\sigma_{n-1}(t)).$$

458 We can then use repeated applications of Equations ?? and ?? in order to obtain a synthetic dataset.

459 When the template first-order correlations are constructed to exhibit different temporal profiles (e.g.,  
460 using the constant, random, ramping, and event procedures described above), (for  $n > 1$ ) by taking a draw  
461 from  $\mathcal{N}(0, m_n)$  and reshaping the resulting vector to have square dimensions. Intuitively, the resulting  
462 re-shaped matrix will look like a noisy version of the template matrix,  $m_{n-1}$ . (When  $n = 1$ , no re-shaping

463 is needed; the resulting  $K$ -dimensional vector may be used as the observation at the given timepoint.)  
464 After independently drawing each timepoint's order  $n - 1$  correlation matrix from that timepoint's order  
465  $n$  correlation matrix, this process can be applied repeatedly until  $n = 0$ . This results in a  $K$ -dimensional  
466 timeseries of  $T$  observations containing the specified high-order correlations and synthetic data will exhibit  
467 the same category of temporal profile at orders 1 through  $n$ . Following our approach to generating synthetic  
468 data exhibiting known first-order correlations, we constructed a total of 40–400 additional multivariate  
469 timeseries, collectively reflecting a total of 4 qualitatively different patterns of dynamic correlations (i.e.,  
470 10–100 datasets reflecting each type of dynamic pattern: constant, random, ramping, and event). Each  
471 timeseries comprised 10 zero-order features (dimensions) that varied over 300 timepoints. After applying  
472 our dynamic correlation estimation procedure, this yielded a 100-dimensional timeseries of first-order  
473 features that could then be used to estimate dynamic second-order correlations. (We chose to use  $K = 10$   
474 zero-order features for our higher order simulations in order to put the accuracy computations displayed  
475 in Figs. 2 and 3 on a roughly even footing.)

#### 476 Functional neuroimaging data collected during story listening

477 We examined an fMRI dataset collected by Simony et al. (2016) that the authors have made publicly available  
478 at [arks.princeton.edu/ark:/88435/dsp015d86p269k](https://arks.princeton.edu/ark:/88435/dsp015d86p269k). The dataset comprises neuroimaging data collected as  
479 participants listened to an audio recording of a story (intact condition; 36 participants), listened to temporally  
480 scrambled recordings of the same story (17 participants in the paragraph-scrambled condition listened to  
481 the paragraphs in a randomized order and 36 in the word-scrambled condition listened to the words in a  
482 randomized order), or lay resting with their eyes open in the scanner (rest condition; 36 participants). Full  
483 neuroimaging details may be found in the original paper for which the data were collected (Simony et al.,  
484 2016).

485 **Hierarchical topographic factor analysis (HTFA).** Following our prior related work, we used HTFA (Manning et al., 2018) to derive a compact representation of the neuroimaging data. In brief, this approach approximates the timeseries of voxel activations (44,415 voxels) using a much smaller number of radial basis function (RBF) nodes (in this case, 700 nodes, as determined by an optimization procedure described by Manning et al., 2018). This provides a convenient representation for examining full-brain network dynamics.  
486 All of the analyses we carried out on the neuroimaging dataset were performed in this lower-dimensional  
487 space. In other words, each participant's data matrix,  $X_0$ , was a number-of-timepoints by 700 matrix of  
488 HTFA-derived factor weights (where the row and column labels were matched across participants). Code  
489 for carrying out HTFA on fMRI data may be found as part of the BrainIAK toolbox (Capota et al., 2017),

494 which may be downloaded at [brainiak.org](http://brainiak.org).

495 **Temporal decoding**

496 We sought to identify neural patterns that reflected participants' ongoing cognitive processing of incoming  
497 stimulus information. As reviewed by Simony et al. (2016), one way of homing in on these stimulus-driven  
498 neural patterns is to compare activity patterns across individuals (e.g., using ISFC analyses). In particular,  
499 neural patterns will be similar across individuals to the extent that the neural patterns under consideration  
500 are stimulus-driven, and to the extent that the corresponding cognitive representations are reflected in  
501 similar spatial patterns across people (also see Simony & Chang, 2020). Following this logic, we used an  
502 across-participant temporal decoding test developed by Manning et al. (2018) to assess the degree to which  
503 different neural patterns reflected ongoing stimulus-driven cognitive processing across people (Fig. 10). The  
504 approach entails using a subset of the data to train a classifier to decode stimulus timepoints (i.e., moments  
505 in the story participants listened to) from neural patterns. We use decoding (forward inference) accuracy  
506 on held-out data, from held-out participants, as a proxy for the extent to which the inputted neural patterns  
507 reflected stimulus-driven cognitive processing in a similar way across individuals.

508 **Forward inference and decoding accuracy**

509 We used an across-participant correlation-based classifier to decode which stimulus timepoint matched  
510 each timepoint's neural pattern (Fig. 10). We first divided the participants into two groups: a template group,  
511  $\mathcal{G}_{\text{template}}$  (i.e., training data), and a to-be-decoded group,  $\mathcal{G}_{\text{decode}}$  (i.e., test data). We used Equation 7 to  
512 compute a DISFC matrix for each group ( $\bar{\mathbf{C}}_{\text{template}}$  and  $\bar{\mathbf{C}}_{\text{decode}}$ , respectively). We then correlated the rows of  
513  $\bar{\mathbf{C}}_{\text{template}}$  and  $\bar{\mathbf{C}}_{\text{decode}}$  to form a number-of-timepoints by number-of-timepoints decoding matrix,  $\Lambda$ . In this  
514 way, the rows of  $\Lambda$  reflected timepoints from the template group, while the columns reflected timepoints  
515 from the to-be-decoded group. We used  $\Lambda$  to assign temporal labels to each row  $\bar{\mathbf{C}}_{\text{decode}}$  using the row of  
516  $\bar{\mathbf{C}}_{\text{template}}$  with which it was most highly correlated. We then repeated this decoding procedure, but using  
517  $\mathcal{G}_{\text{decode}}$  as the template group and  $\mathcal{G}_{\text{template}}$  as the to-be-decoded group. Given the true timepoint labels (for  
518 each group), we defined the *decoding accuracy* as the average proportion of correctly decoded timepoints,  
519 across both groups. We defined the *relative decoding accuracy* as the difference between the decoding accuracy  
520 and chance accuracy (i.e.,  $\frac{1}{T}$ ).

521 **Feature weighting and testing**

522 We sought to examine which types of neural features (i.e., activations, first-order dynamic correlations, and  
523 higher-order dynamic correlations) were informative to the temporal decoders. Using the notation above,  
524 these features correspond to  $\mathbf{X}_0, \mathbf{X}_1, \mathbf{X}_2, \mathbf{X}_3$ , and so on.

525 One challenge to fairly evaluating high-order correlations is that if the kernel used in Equation 4 is  
526 wider than a single timepoint, each repeated application of the equation will result in further temporal  
527 blur. Because our primary assessment metric is temporal decoding accuracy, this unfairly biases against  
528 detecting meaningful signal in higher-order correlations (relative to lower-order correlations). We attempted  
529 to mitigate temporal blur in estimating each  $\mathbf{X}_n$  by using a Dirac  $\delta$  function kernel (which places all of its  
530 mass over a single timepoint; Fig. 9b, 10a) to compute each lower-order correlation ( $\mathbf{X}_1, \mathbf{X}_2, \dots, \mathbf{X}_{n-1}$ ). We  
531 then used a new (potentially wider, as described below) kernel to compute  $\mathbf{X}_n$  from  $\mathbf{X}_{n-1}$ . In this way,  
532 temporal blurring was applied only in the last step of computing  $\mathbf{X}_n$ . We note that, because each  $\mathbf{X}_n$  is a  
533 low-dimensional representation of the corresponding  $\mathbf{Y}_n$ , the higher-order correlations we estimated reflect  
534 true correlations in the data with lower-fidelity than estimates of lower-order correlations. Therefore, even  
535 after correcting for temporal blurring, our approach is still biased against finding meaningful signal in  
536 higher-order correlations.

537 After computing each  $\mathbf{X}_1, \mathbf{X}_2, \dots, \mathbf{X}_{n-1}$  for each participant, we divided participants into two equally sized  
538 groups ( $\pm 1$  for odd numbers of participants):  $\mathcal{G}_{\text{train}}$  and  $\mathcal{G}_{\text{test}}$ . We then further subdivided  $\mathcal{G}_{\text{train}}$  into  $\mathcal{G}_{\text{train}_1}$   
539 and  $\mathcal{G}_{\text{train}_2}$ . We then computed  $\Lambda$  (temporal correlation) matrices for each type of neural feature, using  $\mathcal{G}_{\text{train}_1}$   
540 and  $\mathcal{G}_{\text{train}_2}$ . This resulted in  $n + 1$   $\Lambda$  matrices (one for the original timeseries of neural activations, and one  
541 for each of  $n$  orders of dynamic correlations). Our objective was to find a set of weights for each of these  
542  $\Lambda$  matrices such that the weighted average of the  $n + 1$  matrices yielded the highest decoding accuracy.  
543 We used quasi-Newton gradient ascent (Nocedal & Wright, 2006), using decoding accuracy (for  $\mathcal{G}_{\text{train}_1}$  and  
544  $\mathcal{G}_{\text{train}_2}$ ) as the objective function to be maximized, to find an optimal set of training data-derived weights,  
545  $\phi_{0,1,\dots,n}$ , where  $\sum_{i=0}^n \phi_i = 1$  and where  $\phi_i \geq 0 \forall i \in [0, 1, \dots, n]$ .

546 After estimating an optimal set of weights, we computed a new set of  $n + 1$   $\Lambda$  matrices correlating the  
547 DISFC patterns from  $\mathcal{G}_{\text{train}}$  and  $\mathcal{G}_{\text{test}}$  at each timepoint. We use the resulting decoding accuracy of  $\mathcal{G}_{\text{test}}$   
548 timepoints (using the weights in  $\phi_{0,1,\dots,n}$  to average the  $\Lambda$  matrices) to estimate how informative the set of  
549 neural features containing up to  $n^{\text{th}}$  order correlations were.

550 We used a permutation-based procedure to form stable estimates of decoding accuracy for each set of  
551 neural features. In particular, we computed the decoding accuracy for each of 10 random group assignments  
552 of  $\mathcal{G}_{\text{train}}$  and  $\mathcal{G}_{\text{test}}$ . We report the mean accuracy (along with 95% confidence intervals) for each set of neural

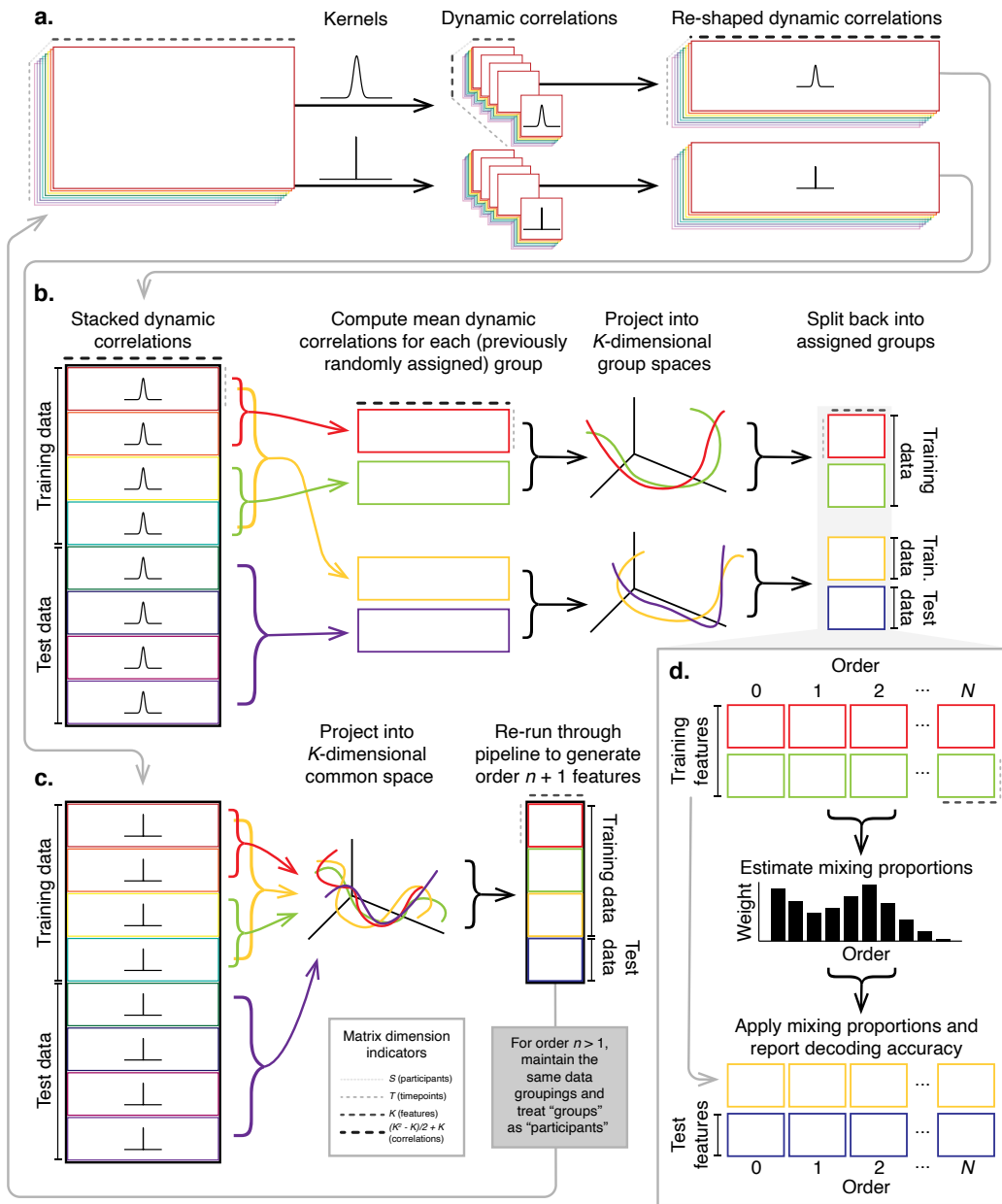


**Figure 10: Decoding analysis pipeline.** **a. Computing dynamic correlations from timeseries data.** Given a timeseries of observations as a  $T \times K$  matrix (or a set of  $S$  such matrices), we use Equation 4 to compute each participant's DISFC (relative to other participants in the training or test sub-group, as appropriate). We repeat this process twice—once using the analysis kernel (shown here as a Gaussian in the upper row of the panel), and once using a  $\delta$  function kernel (lower row of the panel). **b. Projecting dynamic correlations into a lower-dimensional space.** We project the training and test data into  $K$ -dimensional spaces to create compact representations of dynamic correlations at the given order (estimated using the analysis kernel). **c. Kernel trick.** We project the dynamic correlations computed using a  $\delta$  function kernel into a common  $K$ -dimensional space. These low-dimensional embeddings are fed back through the analysis pipeline in order to compute features at the next-highest order. **d. Decoding analysis.** We split the training data into two equal groups, and optimize the feature weights (i.e., dynamic correlations at each order) to maximize decoding accuracy. We then apply the trained classifier to the (held-out) test data.

553 features.

554 **Identifying robust decoding results**

555 The temporal decoding procedure we use to estimate which neural features support ongoing cognitive  
556 processing is governed by several parameters. In particular, Equation 4 requires defining a kernel function,  
557 which can take on different shapes and widths. For a fixed set of neural features, each of these parameters  
558 can yield different decoding accuracies. Further, the best decoding accuracy for a given timepoint may be  
559 reliably achieved by one set of parameters, whereas the best decoding accuracy for another timepoint might  
560 be reliably achieved by a different set of parameters, and the best decoding accuracy across *all* timepoints  
561 might be reliably achieved by still another different set of parameters. Rather than attempting to maximize  
562 decoding accuracy, we sought to discover the trends in the data that were robust to classifier parameters  
563 choices. Specifically, we sought to characterize how decoding accuracy varied (under different experimental  
564 conditions) as a function of which neural features were considered.

565 To identify decoding results that were robust to specific classifier parameter choices, we repeated our  
566 decoding analyses after substituting into Equation 4 each of a variety of kernel shapes and widths. We  
567 examined Gaussian (Fig. 9c), Laplace (Fig. 9d), and Mexican Hat (Fig. 9e) kernels, each with widths of 5, 10,  
568 20, and 50 samples. We then report the average decoding accuracies across all of these parameter choices.  
569 This enabled us to (partially) factor out performance characteristics that were parameter-dependent, within  
570 the set of parameters we examined.

571 **Reverse inference**

572 The dynamic patterns we examined comprise high-dimensional correlation patterns at each timepoint. To  
573 help interpret the resulting patterns in the context of other studies, we created summary maps by computing  
574 the across-timepoint average pairwise correlations at each order of analysis (first order, second order, etc.).  
575 We selected the 10 strongest (absolute value) correlations at each order. Each correlation is between the  
576 dynamic activity patterns (or patterns of dynamic high-order correlations) measured at two RBF nodes  
577 (see *Hierarchical Topographic Factor Analysis*). Therefore, the 10 strongest correlations involved up to 20 RBF  
578 nodes. Each RBF defines a spatial function whose activations range from 0 to 1. We constructed a map  
579 of RBF components that denoted the endpoints of the 10 strongest correlations (we set each RBF to have a  
580 maximum value of 1). We then carried out a meta analysis using Neurosynth (Rubin et al., 2017) to identify  
581 the 10 terms most commonly associated with the given map. This resulted in a set of 10 terms associated  
582 with the average dynamic correlation patterns at each order.

583 **Acknowledgements**

584 We acknowledge discussions with Luke Chang, Vassiki Chauhan, Hany Farid, Paxton Fitzpatrick, Andrew  
585 Heusser, Eshin Jolly, Aaron Lee, Qiang Liu, Matthijs van der Meer, Judith Mildner, Gina Notaro, Stephen  
586 Satterthwaite, Emily Whitaker, Weizhen Xie, and Kirsten Ziman. Our work was supported in part by NSF  
587 EPSCoR Award Number 1632738 to J.R.M. and by a sub-award of DARPA RAM Cooperative Agreement  
588 N66001-14-2-4-032 to J.R.M. The content is solely the responsibility of the authors and does not necessarily  
589 represent the official views of our supporting organizations.

590 **Author contributions**

591 Concept: J.R.M. Implementation: T.H.C., L.L.W.O., and J.R.M. Analyses: L.L.W.O. and J.R.M. Writing:  
592 L.L.W.O. and J.R.M.

593 **References**

- 594 Allen, E. A., Damaraju, E., Plis, S. M., Erhardt, E. B., Eichele, T., & Calhoun, V. D. (2012). Tracking  
595 whole-brain connectivity dynamics in the resting state. *Cerebral Cortex*, 24(3), 663–676.
- 596 Alvarez-Hamelin, I., Dall’Asta, L., Barrat, A., & Vespignani, A. (2005). *k*-corr decomposition: a tool for the  
597 visualization of large scale networks. *arXiv*, cs/0504107v2.
- 598 Baldassano, C., Chen, J., Zadbood, A., Pillow, J. W., Hasson, U., & Norman, K. A. (2017). Discovering event  
599 structure in continuous narrative perception and memory. *Neuron*, 95(3), 709–721.
- 600 Barthélémy, M. (2004). Betweenness centrality in large complex networks. *European Physical Journal B*, 38,  
601 163–168.
- 602 Bassett, D., Meyer-Lindenberg, A., Achard, S., Duke, T., & Bullmore, E. (2006). Adaptive reconfiguration  
603 of fractal small-world human brain functional networks. *Proceedings of the National Academy of Sciences,*  
604 USA, 103(51), 19518–19523.
- 605 Beaty, R. E., Benedek, M., Silvia, P. J., & Schacter, D. L. (2016). Creative cognition and brain network  
606 dynamics. *Trends in Cognitive Sciences*, 20(2), 87–95.
- 607 Betzel, R. F., Byrge, L., Esfahlani, F. Z., & Kennedy, D. P. (2019). Temporal fluctuations in the brain’s modular  
608 architecture during movie-watching. *bioRxiv*, doi.org/10.1101/750919.

- 609 Bonacich, P. (2007). Some unique properties of eigenvector centrality. *Social Networks*, 29(4), 555–564.
- 610 Bressler, S. L., & Kelso, J. A. S. (2001). Cortical coordination dynamics and cognition. *Trends in Cognitive Sciences*, 5(1), 26–36.
- 612 Bullmore, E., & Sporns, O. (2009). Complex brain networks: graph theoretical analysis of structural and  
613 functional systems. *Nature Reviews Neuroscience*, 10(3), 186–198.
- 614 Capota, M., Turek, J., Chen, P.-H., Zhu, X., Manning, J. R., Sundaram, N., . . . Shin, Y. S. (2017). *Brain imaging  
615 analysis kit*.
- 616 Chang, C., & Glover, G. H. (2010). Time-frequency dynamics of resting-state brain connectivity measured  
617 with fMRI. *NeuroImage*, 50, 81–98.
- 618 Chien, H.-Y. S., & Honey, C. J. (2019). Constructing and forgetting temporal context in the human cerebral  
619 cortex. *bioRxiv*, doi.org/10.1101/761593.
- 620 Christakis, N. A., & Fowler, J. H. (2010). Social network sensors for early detection of contagious outbreaks.  
621 *PLoS One*, 5(9), e12948.
- 622 Combrisson, E., Vallat, R., O'Reilly, C., Jas, M., Pascarella, A., l Saive, A., . . . Jerbi, K. (2019). Visbrain: a  
623 multi-purpose GPU-accelerated open-source suite for multimodal brain data visualization. *Frontiers in  
624 Neuroinformatics*, 13(14), 1–14.
- 625 Comon, P., Jutten, C., & Herault, J. (1991). Blind separation of sources, part II: problems statement. *Signal  
626 Processing*, 24(1), 11–20.
- 627 Demertzi, A., Tagliazucchi, E., Dehaene, S., Deco, G., Barttfeld, P., Raimondo, F., . . . Sitt, J. D. (2019). Human  
628 consciousness is supported by dynamic complex patterns of brain signal coordination. *Science Advances*,  
629 5(2), eaat7603.
- 630 Estrada, E., & Rodríguez-Velázquez, J. A. (2005). Subgraph centrality in complex networks. *Physical Review  
631 E*, 71(5), 056103.
- 632 Etzel, J. A., Gazzola, V., & Keysers, C. (2009). An introduction to anatomical ROI-based fMRI classification.  
633 *Brain Research*, 1281, 114–125.
- 634 Fallon, J., Ward, P. G. D., Parkes, L., & Oldham, S. (2020). Timescales of spontaneous fMRI fluctuations  
635 relate to structural connectivity in the brain. *Network Neuroscience*, 4(3), 788–806.

- 636 Fong, A. H. C., Yoo, K., Rosenberg, M. D., Zhang, S., Li, C.-S. R., Scheinost, D., ... Chun, M. M. (2019).  
637 Dynamic functional connectivity during task performance and rest predicts individual differences in  
638 attention across studies. *NeuroImage*, 188, 14–25.
- 639 Freeman, L. C. (1977). A set of measures of centrality based on betweenness. *Sociometry*, 40(1), 35–41.
- 640 Friston, K. J. (2000). The labile brain. I. neuronal transients and nonlinear coupling. *Philosophical Transactions of the Royal Society of London*, 355B, 215–236.
- 641
- 642 Geisberger, R., Sanders, P., & Schultes, D. (2008). Better approximation of betweenness centrality. *Proceedings of the Meeting on Algorithm Engineering and Experiments*, 90–100.
- 643
- 644 Gershman, S. J., Blei, D. M., Pereira, F., & Norman, K. A. (2011). A topographic latent source model for  
645 fMRI data. *NeuroImage*, 57, 89–100.
- 646 Gonzalez-Castillo, J., Caballero-Gaudes, C., Topolski, N., Handwerker, D. A., Pereira, F., & Bandettini, P. A.  
647 (2019). Imaging the spontaneous flow of thought: distinct periods of cognition contribute to dynamic  
648 functional connectivity during rest. *NeuroImage*, 202(116129).
- 649 Grossberg, S. (1988). Nonlinear neural networks: principles, mechanisms, and architectures. *Neural Networks*, 1(1), 17–61.
- 650
- 651 Halu, A., Mondragón, R. J., Panzarasa, P., & Bianconi, G. (2013). Multiplex PageRank. *PLoS One*, 8(10),  
652 e78293.
- 653 Hasson, U., Chen, J., & Honey, C. J. (2015). Hierarchical process memory: memory as an integral component  
654 of information processing. *Trends in Cognitive Sciences*, 19(6), 304–315.
- 655 Hasson, U., Yang, E., Vallines, I., Heeger, D. J., & Rubin, N. (2008). A hierarchy of temporal receptive  
656 windows in human cortex. *The Journal of Neuroscience*, 28(10), 2539–2550.
- 657 Haxby, J. V., Gobbini, M. I., Furey, M. L., Ishai, A., Schouten, J. L., & Pietrini, P. (2001). Distributed and  
658 overlapping representations of faces and objects in ventral temporal cortex. *Science*, 293, 2425–2430.
- 659 Hinton, G. E., & Salakhutdinov, R. R. (2006). Reducing the dimensionality of data with neural networks.  
660 *Science*, 313(5786), 504–507.
- 661 Honey, C. J., Kotter, R., Breakspear, M., & Sporns, O. (2007). Network structure of cerebral cortex shapes  
662 functional connectivity on multiple time scales. *Proceedings of the National Academy of Sciences, USA*,  
663 104(24), 10240–10245.

- 664 Honey, C. J., Thesen, T., Donner, T. H., Silbert, L. J., Carlson, C. E., Devinsky, O., ... Hasson, U. (2012). Slow  
665 cortical dynamics and the accumulation of information over long timescales. *Neuron*, 76, 423–434.
- 666 Huth, A. G., de Heer, W. A., Griffiths, T. L., Theunissen, F. E., & Gallant, J. L. (2016). Natural speech reveals  
667 the semantic maps that tile human cerebral cortex. *Nature*, 532, 453–458.
- 668 Huth, A. G., Nisimoto, S., Vu, A. T., & Gallant, J. L. (2012). A continuous semantic space describes  
669 the representation of thousands of object and action categories across the human brain. *Neuron*, 76(6),  
670 1210–1224.
- 671 Jutten, C., & Herault, J. (1991). Blind separation of sources, part I: an adaptive algorithm based on  
672 neuromimetic architecture. *Signal Processing*, 24(1), 1–10.
- 673 Kamitani, Y., & Tong, F. (2005). Decoding the visual and subjective contents of the human brain. *Nature  
674 Neuroscience*, 8, 679–685.
- 675 Landau, E. (1895). Zur relativen Wertbemessung der Turnierresultate. *Deutsches Wochenschach*, 11, 366–369.
- 676 Lee, C. S., Aly, M., & Baldassano, C. (2020). Anticipation of temporally structured events in the brain.  
677 *bioRxiv*, 10.1101/2020.10.14.338145.
- 678 Lee, D. D., & Seung, H. S. (1999). Learning the parts of objects by non-negative matrix factorization. *Nature*,  
679 401, 788–791.
- 680 Lerner, Y., Honey, C. J., Katkov, M., & Hasson, U. (2014). Temporal scaling of neural responses to compressed  
681 and dilated natural speech. *Journal of Neurophysiology*, 111, 2433–2444.
- 682 Lerner, Y., Honey, C. J., Silbert, L. J., & Hasson, U. (2011). Topographic mapping of a hierarchy of temporal  
683 receptive windows using a narrated story. *The Journal of Neuroscience*, 31(8), 2906–2915.
- 684 Liégeois, R., Li, J., Kong, R., Orban, C., Van De Ville, D., Ge, T., ... Yeo, B. T. T. (2019). Resting brain  
685 dynamics at different timescales capture distinct aspects of human behavior. *Nature Communications*,  
686 10(2317), 1–9.
- 687 Lin, J. (2009). Divergence measures based on the Shannon entropy. *IEEE Transactions on Information Theory*,  
688 37(1), 145–151.
- 689 Lohmann, G., Margulies, D. S., Horstmann, A., Pleger, B., Lepsius, J., Goldhahn, D., ... Turner, R. (2010).  
690 Eigenvector centrality mapping for analyzing connectivity patterns in fMRI data of the human brain.  
691 *PLoS One*, 5(4), e10232.

- 692 Lurie, D., Kessler, D., Bassett, D., Betzel, R., Breakspear, M., Keilholz, S., ... Calhoun, V. (2018). On the  
693 nature of time-varying functional connectivity in resting fMRI. *PsyArXiv*, doi.org/10.31234/osf.io/xtzre.
- 694 Mack, M. L., Preston, A. R., & Love, B. C. (2017). Medial prefrontal cortex compresses concept representations  
695 through learning. *bioRxiv*, doi.org/10.1101/178145.
- 696 Mairal, J., Ponce, J., Sapiro, G., Zisserman, A., & Bach, F. R. (2009). Supervised dictionary learning. *Advances*  
697 in *Neural Information Processing Systems*, 1033–1040.
- 698 Mairal, J. B., Bach, F., Ponce, J., & Sapiro, G. (2009). Online dictionary learning for sparse coding. *Proceedings*  
699 of the International Conference on Machine Learning, 689–696.
- 700 Manning, J. R., Ranganath, R., Norman, K. A., & Blei, D. M. (2014). Topographic factor analysis: a Bayesian  
701 model for inferring brain networks from neural data. *PLoS One*, 9(5), e94914.
- 702 Manning, J. R., Zhu, X., Willke, T. L., Ranganath, R., Stachenfeld, K., Hasson, U., ... Norman, K. A. (2018).  
703 A probabilistic approach to discovering dynamic full-brain functional connectivity patterns. *NeuroImage*,  
704 180, 243–252.
- 705 McInnes, L., Healy, J., & Melville, J. (2018). UMAP: uniform manifold approximation and projection for  
706 dimension reduction. *arXiv*, 1802(03426).
- 707 McIntosh, A. R. (2000). Towards a network theory of cognition. *Neural Networks*, 13(8–9), 861–870.
- 708 McIntosh, A. R., & Jirsa, V. K. (2019). The hidden repertoire of brain dynamics and dysfunction. *Network*  
709 *Neuroscience*, doi.org/10.1162/netn\_a\_00107.
- 710 Mitchell, T. M., Shinkareva, S. V., Carlson, A., Chang, K. M., Malave, V. L., Mason, R. A., & Just, M. A.  
711 (2008). Predicting human brain activity associated with the meanings of nouns. *Science*, 320(5880), 1191.
- 712 Newman, M. E. J. (2005). A measure of betweenness centrality based on random walks. *Social Networks*, 27,  
713 39–54.
- 714 Newman, M. E. J. (2008). The mathematics of networks. *The New Palgrave Encyclopedia of Economics*, 2, 1–12.
- 715 Nishimoto, S., Vu, A. T., Naselaris, T., Benjamini, Y., Yu, B., & Gallant, J. L. (2011). Reconstructing visual  
716 experience from brain activity evoked by natural movies. *Current Biology*, 21, 1–6.
- 717 Nocedal, J., & Wright, S. J. (2006). *Numerical optimization*. New York, NY: Springer.
- 718 Norman, K. A., Polyn, S. M., Detre, G. J., & Haxby, J. V. (2006). Beyond mind-reading: multi-voxel pattern  
719 analysis of fMRI data. *Trends in Cognitive Sciences*, 10(9), 424–430.

- 720 Opsahl, T., Agneessens, F., & Skvoretz, J. (2010). Node centrality in weighted networks: generalizing degree  
721 and shortest paths. *Social Networks*, 32, 245–251.
- 722 Park, H.-J., Friston, K. J., Pae, C., Park, B., & Razi, A. (2018). Dynamic effective connectivity in resting state  
723 fMRI. *NeuroImage*, 180, 594–608.
- 724 Pearson, K. (1901). On lines and planes of closest fit to systems of points in space. *The London, Edinburgh,  
725 and Dublin Philosophical Magazine and Journal of Science*, 2, 559–572.
- 726 Pereira, F., Lou, B., Pritchett, B., Ritter, S., Gershman, S. J., Kanwisher, N., ... Fedorenko, E. (2018). Toward  
727 a universal decoder of linguistic meaning from brain activation. *Nature Communications*, 9(963), 1–13.
- 728 Preti, M. G., Bolton, T. A. W., & Van De Ville, D. (2017). The dynamic functional connectome: state-of-the-art  
729 and perspectives. *NeuroImage*, 160, 41–54.
- 730 Rao, C. R. (1982). Diversity and dissimilarity coefficients: a unified approach. *Theoretical Population Biology*,  
731 21(1), 24–43.
- 732 Reimann, M. W., Nolte, M., Scolamiero, M., Turner, K., Perin, R., Chindemi, G., ... Markram, H. (2017).  
733 Cliques of neurons bound into cavities provide a missing link between structure and function. *Frontiers  
734 in Computational Neuroscience*, 11(48), 1–16.
- 735 Ricotta, C., & Szeidl, L. (2006). Towards a unifying approach to diversity measures: bridging the gap  
736 between the Shannon entropy and Rao's quadratic index. *Theoretical Population Biology*, 70(3), 237–243.
- 737 Roy, D. S., Park, Y.-G., Ogawa, S. K., Cho, J. H., Choi, H., Kamensky, L., ... Tonegawa, S. (2019). Brain-  
738 wide mapping of contextual fear memory engram ensembles supports the dispersed engram complex  
739 hypothesis. *bioRxiv*, doi.org/10.1101/668483.
- 740 Rubin, T. N., Kyoejo, O., Gorgolewski, K. J., Jones, M. N., Poldrack, R. A., & Yarkoni, T. (2017). Decoding  
741 brain activity using a large-scale probabilistic functional-anatomical atlas of human cognition. *PLoS  
742 Computational Biology*, 13(10), e1005649.
- 743 Rubinov, M., & Sporns, O. (2010). Complex network measures of brain connectivity: uses and interpreta-  
744 tions. *NeuroImage*, 52, 1059–1069.
- 745 Schreiber, T. (2000). Measuring information transfer. *Physical Review Letters*, 85(2), 461–464.
- 746 Shappell, H., Caffo, B. S., Pekar, J. J., & Lindquist, M. A. (2019). Improved state change estimation in  
747 dynamic functional connectivity using hidden semi-Markov models. *NeuroImage*, 191, 243–257.

- 748 Simony, E., & Chang, C. (2020). Analysis of stimulus-induced brain dynamics during naturalistic paradigms.  
749 *NeuroImage*, 216, 116461.
- 750 Simony, E., Honey, C. J., Chen, J., & Hasson, U. (2016). Dynamic reconfiguration of the default mode  
751 network during narrative comprehension. *Nature Communications*, 7(12141), 1–13.
- 752 Sizemore, A. E., Giusti, C., Kahn, A., Vettel, J. M., Betzel, R. F., & Bassett, D. S. (2018). Cliques and cavities  
753 in the human connectome. *Journal of Computational Neuroscience*, 44(1), 115–145.
- 754 Solomon, S. H., Medaglia, J. D., & Thompson-Schill, S. L. (2019). Implementing a concept network model.  
755 *Behavior Research Methods*, 51, 1717–1736.
- 756 Spearman, C. (1904). General intelligence, objectively determined and measured. *American Journal of  
757 Psychology*, 15, 201–292.
- 758 Sporns, O., & Honey, C. J. (2006). Small worlds inside big brains. *Proceedings of the National Academy of  
759 Sciences, USA*, 103(51), 19219–19220.
- 760 Thompson, W. H., Richter, C. G., Plavén-Sigray, P., & Fransson, P. (2018). Simulations to benchmark  
761 time-varying connectivity methods for fMRI. *PLoS Computational Biology*, 14(5), e1006196.
- 762 Tipping, M. E., & Bishop, C. M. (1999). Probabilistic principal component analysis. *Journal of Royal Statistical  
763 Society, Series B*, 61(3), 611–622.
- 764 Toker, D., & Sommer, F. T. (2019). Information integration in large brain networks. *PLoS Computational  
765 Biology*, 15(2), e1006807.
- 766 Tong, F., & Pratte, M. S. (2012). Decoding patterns of human brain activity. *Annual Review of Psychology*, 63,  
767 483–509.
- 768 Turk-Browne, N. B. (2013). Functional interactions as big data in the human brain. *Science*, 342, 580–584.
- 769 van der Maaten, L. J. P., & Hinton, G. E. (2008). Visualizing high-dimensional data using t-SNE. *Journal of  
770 Machine Learning Research*, 9, 2579–2605.
- 771 Vidaurre, D., Abeysuriya, R., Becker, R., Quinn, A. J., Alfaro-Almagro, F., Smith, S. M., & Woolrich, M. W.  
772 (2018). Discovering dynamic brain networks from big data in rest and task. *NeuroImage*, 180, 646–656.
- 773 Zar, J. H. (2010). *Biostatistical analysis*. Prentice-Hall.
- 774 Zheng, M., Allard, A., Hagmann, P., & Serrano, M. . . A. (2019). Geometric renormalization unravels  
775 self-similarity of the multiscale human connectome. *arXiv*, 1904.11793.

776 Zou, Y., Donner, R. V., Marwan, N., Donges, J. F., & Kurths, J. (2019). Complex network approaches to  
777 nonlinear time series analysis. *Physics Reports*, 787, 1–97.